Journal of
Applied Physics

ARTICLE

pubs.aip.org/aip/jap

Defect-specific compensation and redistribution of Si in GaAs:Si structures resolved at subnanometer scale

Cite as: J. Appl. Phys. **138**, 205701 (2025); doi: 10.1063/5.0281923
Submitted: 22 May 2025 · Accepted: 3 November 2025 ·
Published Online: 25 November 2025

View Online Export Citation CrossMark

Adrianna Rejmer,[1,2,a)] Ayse Ozcan-Atar,[3] Walery Kołkowski,[4] Iwona Pasternak,[2] Sylwia Kozdra,[1] Andrzej Materna,[5] Emanuele Pelucchi,[3] Włodzimierz Strupiński,[2,4] and Paweł Piotr Michałowski[1]

AFFILIATIONS

[1]Łukasiewicz Research Network—Institute of Microelectronics and Photonics, Aleja Lotników 32/46, 02-668 Warsaw, Poland
[2]Faculty of Physics, Warsaw University of Technology, Koszykowa 75, 00-662 Warsaw, Poland
[3]Tyndall National Institute, University College Cork, Lee Maltings Complex Dyke Parade, T12 R5CP Cork, Ireland
[4]VIGO Photonics S.A., Poznańska 129/133, 05-850 Ożarów Mazowiecki, Poland
[5]ENSEMBLE3 Sp. z o.o., Wólczyńska 133, 01-919 Warsaw, Poland

[a)]**Author to whom correspondence should be addressed:** Adrianna.Rejmer@imif.lukasiewicz.gov.pl

ABSTRACT

Although the behavior of silicon (Si) in gallium arsenide (GaAs) has been extensively studied, a comprehensive understanding of compensation mechanisms and defect dynamics remains an active area of research. Moreover, a methodological gap persists between atomic-scale defect identification and quantitative depth profiling across technologically relevant device architectures. In this study, we investigated a GaAs/GaAs:Si/GaAs multilayer structure grown by metalorganic vapor phase epitaxy, along with calibration samples of varying silicon concentrations, using a combined approach of Ultra Low Impact Energy Secondary Ion Mass Spectrometry (SIMS) and Electrochemical Capacitance–Voltage profiling. To our knowledge, this work provides the first quantitative depth profiles of individual silicon-related defects—including Si_{Ga}, Si_{As}, Si_{Ga}–Si_{As} pairs, and $Si_{Ga}V_{Ga}$ complexes—with subnanometer resolution. Polyatomic species specific to these defects were identified, enabling SIMS signals to be linked directly to carrier concentration. A calibration strategy integrating a material-specific defect model with experimental profiles was developed, unlocking quantification of defect distributions solely based on SIMS data. Post-growth annealing (800–1000 °C) revealed defects, redistribution, and diffusion behavior, allowing the extraction of diffusion parameters for Si_{Ga} and Si pairs species. Our findings establish a quantitative framework for disentangling the individual contributions of silicon-based defects to compensation effects in GaAs:Si.

I. INTRODUCTION

Silicon-doped gallium arsenide (GaAs:Si) remains an important material in high-frequency electronics and infrared optoelectronics, where its combination of high electron mobility and tunable doping makes it well-suited for applications, such as high-electron-mobility transistors (HEMTs) and optoelectronic devices. Although technological advances have enabled practical workarounds for some limitations associated with GaAs:Si, particularly in device fabrication, there remains ongoing interest in fundamental studies aimed at understanding the microscopic origins of compensation and defect-related behavior. Such insights are especially valuable in addressing persistent challenges, such as achieving low-resistance ohmic contacts suitable for plasmoelectronic devices.[1]

Efficient doping of gallium arsenide with silicon is hindered by compensation effects inherent to this material system. Silicon in GaAs exhibits amphoteric behavior, meaning it can occupy either gallium sites (Si_{Ga}), acting as a donor, or arsenic sites (Si_{As}), acting as an acceptor.[2–5] However, the amphoteric nature of silicon alone does not fully explain the observed limited carrier concentration.[6,7] Beyond this intrinsic self-compensation, additional mechanisms have been identified that further suppress electrical activity at high doping levels. These include the formation of electrically neutral silicon pairs (Si_p), composed of neighboring donor–acceptor pairs (Si_{Ga}–Si_{As}),[7–9] and negatively charged silicon-vacancy complexes $Si_{Ga}V_{Ga}^{2-}$,[2,10–14] which are thought to originate from Coulombic attraction between Si_{Ga}^{+} donors and triply negatively charged gallium vacancies (V_{Ga}^{3-}).[2] Although the active carrier concentration in Si-doped GaAs is known to saturate at approximately $5 \times 10^{18}\ \mathrm{cm}^{-3}$,[7,15,16] a quantitative, depth-resolved characterization of individual silicon-based defects in this material has, to our knowledge, not yet been achieved.

Understanding the distribution and chemical identity of Si-based defects in GaAs is hindered by the limitations of commonly used characterization methods. For instance, carrier concentration profiling techniques, such as electrochemical capacitance–voltage (ECV) measurements, provide only collective information on the depth distribution of free carriers, without insight into the specific defect species responsible for compensation effects.[17] Scanning tunneling microscopy (STM), which has been successfully employed for the identification and quantitative estimation of Si-related defects in GaAs, offers high spatial resolution and sensitivity.[2,18–20] However, while cross-sectional STM on cleaved surfaces can resolve depth profiles across multilayer structures or at buried interfaces, the technique's primary limitation for quantitative analysis is statistical, as its reliance on counting individual dopants over small areas makes obtaining representative data a significant challenge. Although many characterization methods have contributed valuable insights,[2,9,13,14,18,21–24] the precise lattice site dynamics and coordination environments of Si atoms in heavily doped GaAs are not yet fully understood.

Among the standard techniques for depth profiling, Secondary Ion Mass Spectrometry (SIMS) is widely used; however, its historical inability to differentiate between defect types with distinct chemical characteristics limits its applicability for defect-specific analysis. To address this limitation, Ultra Low Impact Energy Secondary Ion Mass Spectrometry (ULIE-SIMS) has emerged as a promising alternative, operating at primary ion energies in the 90–150 eV range.[25] At these energies, the sputtering mechanism differs fundamentally from that in conventional high-energy SIMS, enabling the emission and detection of intact polyatomic cluster ions retains chemical bonding information.[25] Previous studies have demonstrated the capability of ULIE-SIMS to provide meaningful qualitative information about electrically active impurities in semiconductor structures,[26,27] such as zinc-doped GaAs/AlGaAs system where polyatomic ion signals reflected substitutional Zn atoms acting as acceptors.[26] However, in the case of Si, the amphoteric behavior and the presence of multiple compensating configurations significantly complicate the methodological landscape. These factors prevent the use of a single, uniquely identifiable SIMS signal to represent electrically active silicon. Moreover, previously used calibration strategies—such as correlating a single ULIE-SIMS signal with carrier concentration—become less straightforward when a significant fraction of the dopant is self-compensated.

We present a ULIE-SIMS-based approach for the quantitative analysis of individual silicon-based defects in GaAs, enabling depth distribution probing of Si_{Ga}, Si_{As}, Si_p, and $Si_{Ga}V_{Ga}$ defect complexes. For this purpose, we investigated a multilayer structure grown by Metalorganic Vapor Phase Epitaxy (MOVPE) consisting of a 500 nm Si-doped GaAs layer embedded between two undoped epitaxial GaAs layers of the same thickness, alongside a series of calibration samples. We identified polyatomic ULIE-SIMS signals associated with specific silicon-based defect species. Their physical relevance to carrier concentration was then assessed through comparison with ECV profiles. By comparing ULIE-SIMS depth profiles with carrier concentration profiles obtained via ECV measurements, we determined calibration coefficients and derived an empirical formula allowing the extraction of carrier distributions from ULIE-SIMS signals. This approach addresses challenges of a conventional ECV technique, particularly in samples affected by surface degradation or with complex doping profiles and abrupt doping transitions.

The GaAs/GaAs:Si/GaAs structure was subjected to post-growth annealing in the temperature range of 800–1000 °C, enabling the investigation of defect redistribution and diffusion behavior. This approach provided quantitative insights into the contributions of individual defect species to electrical compensation, allowed estimation of diffusion coefficients for Si_{Ga} and Si_p defects, and assessment of the impact of arsenic loss during thermal treatment. By investigating Si-based defect species and their thermal evolution, this study contributes to a deeper understanding of the interplay between dopant diffusion, defect-driven compensation, and carrier saturation phenomena in Si-doped GaAs.

Ultimately, this methodology provides a framework for quantitatively resolving the individual contributions of silicon-based defects to the observed compensation, offering a new predictive tool for optimizing doping and/or activation strategies and ultimately device fabrication in GaAs-based technologies. Moreover, the underlying ULIE-SIMS methodology can potentially be extended to other doped semiconductor systems and complex materials, including emerging semiconductor oxide technologies, such as β-Ga_2O_3.[28] Such oxide semiconductors often pose challenges for conventional characterization techniques, such as ECV measurements, as profiling is typically limited to surface layers due to the material's wide bandgap and related constraints in measurement depth.[29] The ULIE-SIMS approach based on a defect structure could offer a valuable alternative to address these limitations, enabling qualitative defect profiling even when standard electrical characterization methods are limited or impractical. This inherent flexibility positions ULIE-SIMS as a versatile and powerful technique with significant potential for advancing both fundamental materials science and the optimization of early-stage processes in device fabrication.

To facilitate clarity and traceability of the methodological and analytical workflow, we briefly outline the structure of the paper. This overview connects the conceptual framework with the experimental results, calibration steps, and quantitative analyses and leads to the broader discussion of implications. Following Sec. II, Sec. III introduces the defect model, defining the material assumptions used to express total Si content and net carrier concentration in terms of the concentrations and charge states of specific Si-based defects, and then outlines the methodological framework, explaining the rationale for selecting particular ULIE-SIMS signals and their qualitative relationships to defect species based on prior ULIE-SIMS studies. Section IV first presents qualitative ULIE-SIMS profiles for the selected signals (Si, Si_2, As_3Si, and Ga_3Si) in the

GaAs/GaAs:Si/GaAs structure in both as-grown and annealed states, together with SIMS-based assessment of arsenic loss during annealing, and discusses these findings within the adopted framework, including its limitations under As-poor conditions. This is followed by the development and validation, using a dedicated calibration sample set, of an empirical relationship linking carrier concentration to the As_3Si and Ga_3Si signals, yielding calibration coefficients α and β, which are then applied to obtain depth-resolved carrier concentration profiles for the main structures. The empirical carrier–signal equation is next combined with the assumptions of Sec. III to reconstruct quantitative depth profiles for Si_{Ga} and $Si_{Ga}V_{Ga}$, together with directly calibrated profiles for Si_p and an estimate of Si_{As} derived from the physical constraint that $Si_{Ga}V_{Ga}$ concentrations must remain non-negative; all calibration parameters and their physical interpretations are summarized. This framework is then applied to generate complete depth distributions for all considered defects and total Si, and the evolution of these profiles in as-grown and annealed samples is analyzed to extract insights into diffusion and redistribution. Section V interprets these quantitative results in the context of prior literature, evaluates methodological strengths and limitations, and considers the broader implications and future applications of defect analysis using ULIE-SIMS. This paper concludes in Sec. VI with a concise summary of the key findings, the methodological contributions of this work, and the potential for extending the ULIE-SIMS framework to other semiconductor systems.

II. EXPERIMENTAL

A. GaAs/GaAs:Si/GaAs structure

Epitaxial GaAs/GaAs:Si/GaAs structure layers were grown on a 2-in. undoped, single-side-polished GaAs substrate with exact (100) orientation. Growth by MOVPE was performed in an AIX 2800 G4 low pressure horizontal laminar flow reactor with a $12 \times 2''$ configuration. Trimethylgallium (TMGa) was used as the III-group source and arsine (AsH_3) as the group-V source. The real temperature of the wafer surface was 720 °C (monitored using the Laytec *in situ* reflectance measurement system). For n-type doping, silane (SiH_4) diluted in H_2 was used. The growth process entailed three sequential phases: the deposition of a $1\,\mu$m nominally undoped GaAs layer (NUD), the deposition of a $0.5\,\mu$m Si-doped GaAs layer (a total Si concentration of 1.4×10^{19} atoms/cm^3), and the deposition of a $0.5\,\mu$m undoped GaAs layer (NUD). Precise doping was realized thanks to *in situ* mixing of SiH_4 with Pd-purified hydrogen used in the epitaxial process as a carrier gas. Thickness and growth rate were calibrated using SEM cross-sectional analysis and SIMS. After the process, the quality of the sample was assessed with optical microscopy confirming a “mirror-like” surface without visible defects.

B. Calibration samples

Calibration samples (C1–C6) were deliberately grown in a different reactor from the primary GaAs/GaAs:Si/GaAs structure to evaluate the universality of the developed procedure and the consistency of signal calibration across varying growth conditions and equipment. All calibration samples were epitaxially grown on GaAs semi-insulating substrates in a commercial horizontal high purity[30] MOVPE reactor (AIX 200) at low pressure (80 mbar) using purified N_2 as a carrier gas, at a thermocouple temperature of 740 °C. Trimethylgallium (TMGa), arsine (AsH_3), and disilane (Si_2H_6, diluted in N_2) were used as group-III, group-V, and doping precursors, respectively. Thickness and growth rate were calibrated using SEM cross section. After the growth, the quality of the samples was assessed with an optical microscope in a (Nomarski) differential interference contrast (N-DIC) mode ensuring a “mirror-like” surface without defects. The first batch of samples consisted of three samples grown on (100) substrates intentionally misoriented by 0.05° toward the (111)B crystallographic plane (±0.02° tolerance), with varying total Si concentration levels of 9×10^{16} (C1), 4.25×10^{18} (C2), and 4.6×10^{19} atoms/cm^3 (C3), as measured by SIMS based on standard Si calibration samples. The second batch was composed of three samples grown simultaneously on (100) substrates with various intentional misorientations: 0.05° toward a (111)B crystallographic plane (±0.02° tolerance), 0.2° toward a (111)A crystallographic plane (±0.02° tolerance), and 6° toward a (111)A crystallographic plane (±0.1° tolerance), resulting in total Si concentration levels of 9.9×10^{18} (C4), 7.2×10^{18} (C5), and 1.1×10^{19} (C6) atoms/cm^3, respectively.

C. GaAs/GaAs:Si/GaAs annealing

The GaAs/GaAs:Si/GaAs wafer was cleaved into several pieces following growth. Individual pieces were then annealed at temperatures ranging from 800 to 1000 °C, in 50 °C increments, for 30 min each. Annealing was conducted in a horizontal zone furnace under vacuum ($\sim 1 \times 10^{-5}$ mbar), with samples enclosed in sealed quartz ampoules. Samples were protected using a twin-layer GaAs cap, which was placed inside the ampoules to minimize arsenic loss during annealing. This approach was effective up to 950 °C; however, partial arsenic evaporation was observed at 1000 °C, as discussed later in this work. Temperatures were monitored using a calibrated chromel–alumel thermocouple.

D. ULIE-SIMS

In this work, all SIMS measurements were performed employing a CAMECA SC Ultra instrument under ultrahigh vacuum (UHV), usually of 4×10^{-10} mbar. The Cs^+ primary beam was rastered over $150 \times 150\,\mu m^2$ (the analysis area was limited to $100 \times 100\,\mu m^2$). The primary beam had an intensity of 5 nA, with an accelerator voltage of 8000 V, a sample holder voltage of 5000 V, and a floating voltage of 2850 V, resulting in an impact energy of 150 eV at an incidence angle of 75°. These non-standard measurement conditions lead to a very slow erosion rate of approximately 2 nm/min, meaning that each sample was measured for about 14 h. Such long acquisition times require primary beam service, which is carried out in an automatic mode as described in our previous work.[31] The positive ion detection mode was used in most experiments, and thus, all species were measured as CsX^+ cluster ions and point-to-point normalized to Cs^+ signals. The following X signals were measured: Si, Ga_3Si, As_3Si, and Si_2. For simplicity, throughout the remainder of this work if not stated otherwise, the convention is adopted where X refers to the CsX^+ signal. All signals were measured during a single acquisition. However, the extraction parameters were optimized individually for each signal, as also described in our previous work.[31] The Si signal was calibrated using a reference sample (a clean substrate implanted with silicon), and the relative sensitivity factor (RSF) was determined following the well-established approach.[32] For each sample, the matrix signal (Ga) was measured at the end of the experiment by integrating the gallium intensity over 30 s. The resulting values were consistent across all samples, with a relative deviation of only ±0.87%. This high reproducibility allowed the matrix signal dependence to be eliminated, and the calibration factor $h = 1.24 \times 10^{15}$ atoms/cm^3 per count per second to be expressed as an absolute calibration factor. In the case of Si_2, no reference material with known dimer concentration is available. Therefore, an alternative approach was used: the Si_2/Si signal ratio was measured for four distinct solid-state materials, namely, monocrystalline Si, polycrystalline Si, amorphous Si, and $CaSi_2$. All measurements yielded a consistent ratio of 1.88 ± 4%, despite the structural and chemical differences between the samples. This reproducibility justified extrapolation to GaAs-based samples, and the corresponding calibration factor was defined as $h_1 = h/1.88$, and thus, $h_1 = 6.61 \times 10^{14}$ atoms/cm^3 per count per second. The estimation of measurement uncertainty, which involves more complex aspects, is discussed in detail in the Error estimation section of the supplementary material.

E. ECV

Carrier concentration profiles were obtained using a Wafer Profiler CVP21 via standard ECV techniques.[17] For most samples, a large-area sealing ring (10 mm^2) was used to minimize etching edge effects;[17,33,34] in cases of surface degradation after annealing, a smaller ring was employed. ECV measurements on calibration samples were further validated by Hall effect measurements using a Lake Shore Cryotronics 8400 Series HMS system. For GaAs etching, a 0.1 M EDTA in a 0.18 M NaOH electrolyte was used. While measurement accuracy was high for the as-grown and calibration samples, annealed structures exhibited surface roughness that introduced some uncertainty. Considering that the measurements on annealed samples aimed primarily to provide qualitative confirmation of the carrier profiles obtained via ULIE-SIMS, the reduced accuracy was not a critical issue in this part of the study.

III. DEFECT MODEL AND THE MEASUREMENT FRAMEWORK

In this study, we employ SIMS to investigate the distribution of various silicon-based defects in gallium arsenide. The underlying concept of these measurements is to use ultralow energy of the primary ion beam during SIMS bombardment (ULIE-SIMS).[25] It has been demonstrated that for impact energies in the range of 90–150 eV, the sputtering process is significantly different from the standard SIMS experiment (impact energy 1 keV and above). In such a case, each primary ion carries too little energy to effectively break covalent bonds, and therefore, the probability of sputtering larger species is enhanced. Furthermore, the energy transferred from the primary ions is not sufficient to form new bonds between the sputtered species.[25] Therefore, using ULIE-SIMS yields qualitative information about a chemical state, indicating that strong covalent bonds exist between atoms in the sample.[25] In previous works, the method was successfully employed in III–V doped structures, including AlGaA:Zn and InP:Zn, demonstrating that appropriately selected signals from polyatomic ions can provide qualitative information about the distribution of electrically active impurities in semiconductors.[26,27]

To develop a tailored ULIE-SIMS measurement procedure for a specific doped material, it is crucial to select complex signals that can be explicitly interpreted. The case of GaAs:Si is particularly challenging due to the amphoteric nature of silicon in this material and the coexistence of various compensation effects that dominate in different concentration regimes. To address these challenges, a comprehensive approach was employed, combining a material model with a critical evaluation of ULIE-SIMS signal selection and analysis.

A. Defect model

Our considerations are based on several key assumptions, aligned with the commonly reported defect framework for heavily silicon-doped n-type GaAs:Si.[2,9–11,18] We consider four primary types of silicon-related defects: Si_{Ga}^{+} as a donor, $Si_{Ga}V_{Ga}^{2-}$ and Si_{As}^{-} as acceptors, and Si_p as a neutral defect. It is assumed that all silicon atoms are incorporated into the crystal lattice in one of these defect states, and that no interstitial silicon species are present in the material. Consequently, the total silicon concentration [Si] is described by the relationship

$$[\mathrm{Si}] = [\mathrm{Si_{Ga}}] + [\mathrm{Si_{Ga}V_{Ga}}] + [\mathrm{Si_{As}}] + 2[\mathrm{Si_p}], \tag{1}$$

where square brackets represent the concentrations of the respective species. The free-carrier concentration distribution n is assumed to result from the interplay of all charged defects and is given by

$$n = [\mathrm{Si_{Ga}}] - 2[\mathrm{Si_{Ga}V_{Ga}}] - [\mathrm{Si_{As}}]. \tag{2}$$

These assumptions form the basis for the analysis of the behavior of silicon-related defects and their contribution to carrier dynamics in the considered material system.

B. Methodological framework—Selection of ULIE-SIMS signals

The primary criterion for selecting complex signals in ULIE-SIMS studies is the presence of chemical bonds between specific atoms in the analyzed sample. Considering the crystalline structure of GaAs:Si, we have identified three signals: Si_2, Ga_3Si, and As_3Si as promising indicators for characterizing silicon-related defects, specifically Si_p, Si_{As}, Si_{Ga}, and $Si_{Ga}V_{Ga}$. Figure 1 provides a schematic illustration demonstrating the connections between each selected signal and its corresponding defect structure.

The Si_2 signal has an unambiguous interpretation—It reflects the qualitative distribution of silicon pairs in the studied samples. None of the defects considered has a structure competing with silicon pairs (Si_{As}–Si_{Ga} bond), which could complicate signal decoding. Based on previous works[26,27] if the probed species is selected correctly, the intensity of the signal is directly proportional

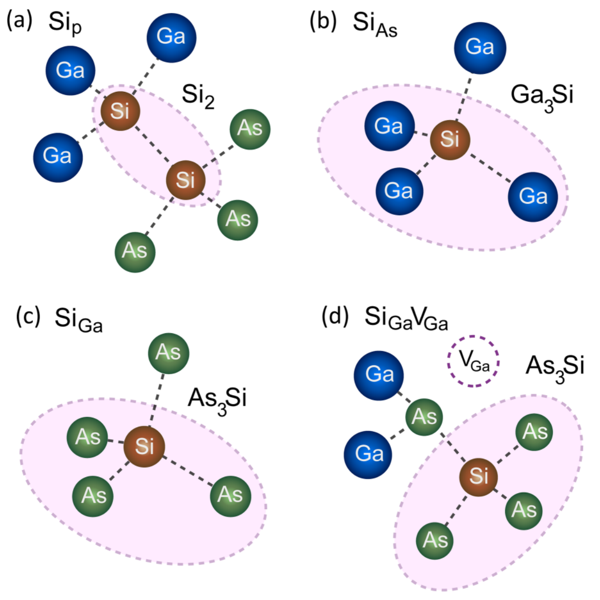

FIG. 1. Schematic representation of the relationship between defect structures and selected ULIE-SIMS signals. The circled areas schematically illustrate the parts of defects chosen to provide information about each defect: (a) Si$_{Ga}$–Si$_{As}$ (Si$_p$)—the selected signal is Si$_2$, (b) Si$_{As}$—the selected signal is Ga$_3$Si, (c) Si$_{Ga}$—the selected signal is As$_3$Si (ambiguous interpretation due to structural similarity with the Si$_{Ga}$V$_{Ga}$ defect), and (d) Si$_{Ga}$V$_{Ga}$—the selected signal is As$_3$Si (ambiguous interpretation due to structural similarity with the Si$_{Ga}$ defect).

to the concentration of the defects being probed. Therefore, we assume that the concentration of silicon pairs [Si$_p$] in the sample is proportional to the intensity of the Si$_2$ signal,

$$\mathrm{Si}_2 \sim [\mathrm{Si}_p]. \tag{3}$$

Similarly, for the Si$_{As}$ defect, where silicon substitutes arsenic, the Si in the crystalline lattice is bonded to gallium. Therefore, the Ga$_3$Si signal (silicon bonded to three gallium atoms) was selected to study the Si$_{As}$ concentration distribution under following assumption:

$$\mathrm{Ga}_3\mathrm{Si} \sim [\mathrm{Si}_{\mathrm{As}}]. \tag{4}$$

The remaining two defects, Si$_{Ga}$ and Si$_{Ga}$V$_{Ga}$, are structurally similar, sharing the common feature of silicon substituting gallium in the crystalline lattice. ULIE-SIMS, by its fundamental nature, is not able to probe vacancies existing in the material, making it impossible to identify a unique signal distinguishing these two defects. However, silicon substituting gallium, whether as a donor or as part of a complex with a vacancy acting as an acceptor, is bonded to arsenic atoms. Therefore, the As$_3$Si signal is a suitable candidate for providing collective information about these defects. Moreover, if the concentration of the Si$_{Ga}$V$_{Ga}$ defect is negligible relative to that of Si$_{Ga}$, a direct proportionality can be expected, similar to the case of uniquely identifiable defects,

$$\mathrm{If}\,[\mathrm{Si}_{\mathrm{Ga}}\mathrm{V}_{\mathrm{Ga}}] \ll [\mathrm{Si}_{\mathrm{Ga}}],\ \mathrm{As}_3\mathrm{Si} \sim [\mathrm{Si}_{\mathrm{Ga}}]. \tag{5}$$

Experiments conducted under ultralow impact energy conditions differ significantly from conventional SIMS experiments; however, the fundamental principles of the SIMS technique remain unchanged. As in classical dynamic SIMS, there is a proportional relationship between the measured secondary ion counts of a species x (I_s^x) and its concentration C_x in the sample. In the case of ULIE-SIMS, by sampling distinctly interpretable CsX$^+$ cluster ions, there exists a proportional relationship between the CsX$^+$ intensity and the structural counterpart of X in the sample.[26,27] However, when selecting a signal whose intensity may be influenced by the presence of multiple species, such as in the case of the As$_3$Si signal originating from Si$_{Ga}$ and Si$_{Ga}$V$_{Ga}$ defects, the situation remains unexplored.

The measured signal intensity is assumed to be an unknown function of the concentrations of the contributing defect species. Specifically, for the As$_3$Si signal, its intensity can be expressed in the most general form as an unknown function f_1 of the concentrations of Si$_{Ga}$ and Si$_{Ga}$V$_{Ga}$ such that

$$\mathrm{As}_3\mathrm{Si} \sim f_1([\mathrm{Si}_{\mathrm{Ga}}], [\mathrm{Si}_{\mathrm{Ga}}\mathrm{V}_{\mathrm{Ga}}]). \tag{6}$$

However, no specific form can be assumed for the function f_1, as there is currently a lack of experimental or theoretical evidence that would permit the deconvolution of signal contributions arising from multiple structurally similar defect species. To date, ULIE-SIMS studies have not addressed this particular challenge, and the mechanisms governing polyatomic signal formation in such cases remain insufficiently characterized.

Alongside the complex signals selected for studying silicon-based defects, the distribution of the total silicon concentration (Si) was also examined by measuring the Si signal intensity (CsSi$^+$), utilizing the standard SIMS capability to quantify overall elemental distributions. This measurement was calibrated using a well-established RSF-based procedure, as described in Sec. II.

IV. RESULTS AND ANALYSIS

A. ULIE-SIMS profiles—A qualitative perspective

Figure 2 presents SIMS depth profiles for GaAs/GaAs:Si/GaAs structures, obtained both before and after annealing at temperatures between 800 and 1000 °C. The measurements of selected Si-based polyatomic species were performed while simultaneously monitoring the total silicon signal (Si).

1. Total Si and Si$_2$

Figure 2(a) displays the qualitative total Si depth profile, which shows a rectangular distribution in the as-grown state, characterized by sharp interfaces and uniform concentration within the doped region. Upon annealing, the profile broadens progressively, consistent with diffusion from an initially rectangular distribution. The Si$_2$ signal [Fig. 2(b)], corresponding to neutral Si$_{Ga}$–Si$_{As}$ pairs (Si$_p$), also exhibits a rectangular profile in the as-grown state. After annealing, the Si$_2$ signal shows minimal changes in both the

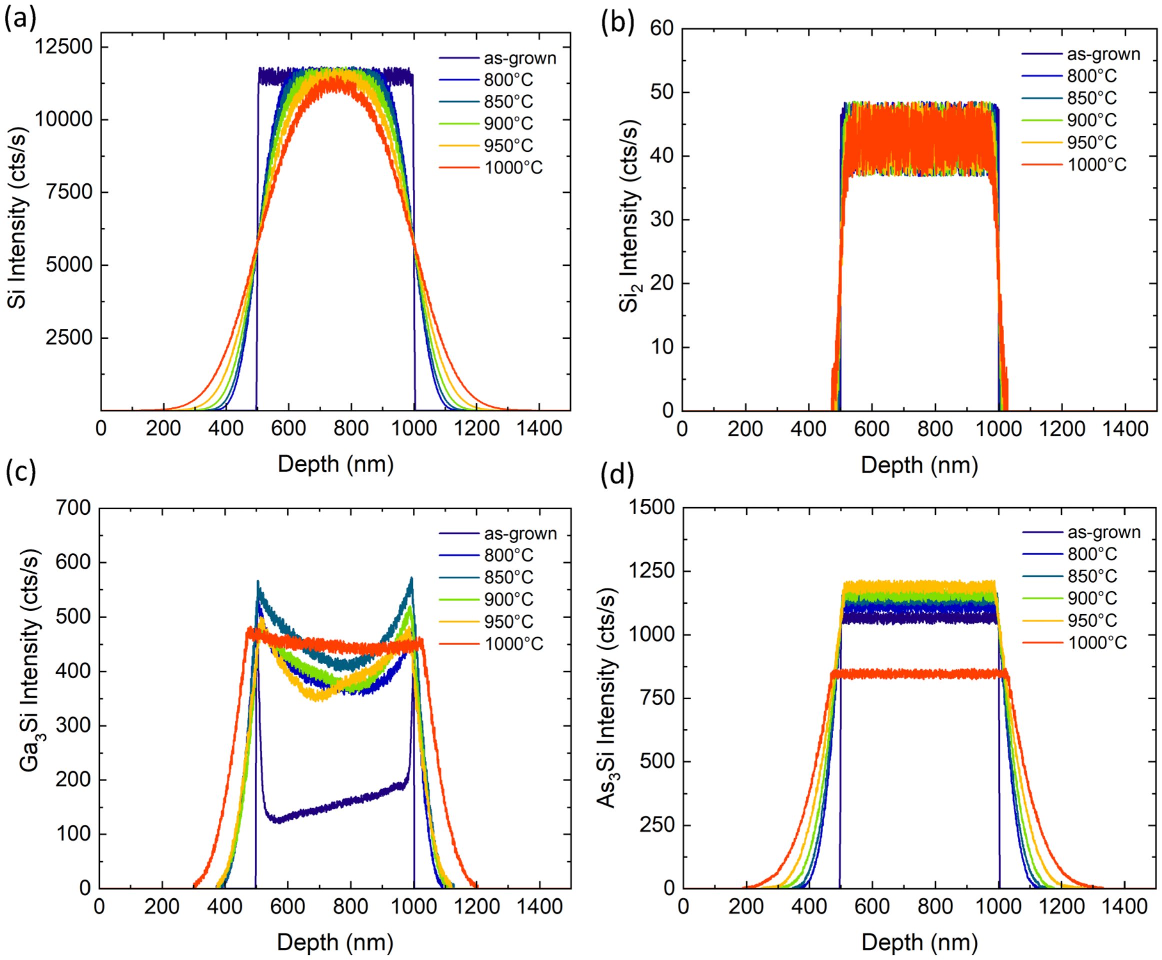

FIG. 2. Depth profiles of all measured Si-based species X where (a) X = Si, (b) X = Si_2, (c) X = Ga_3Si, and (d) X = As_3Si obtained with ULIE-SIMS for a GaAs/GaAs:Si/GaAs structure—as-grown and annealed at (800–1000) °C. All species were measured as CsX^+ cluster ions and point-to-point normalized to Cs^+ signals.

intensity and spatial distribution, even at 1000 °C, remaining confined to the doped region, with no significant broadening or tailing, in contrast to the behavior observed for the total Si signal.

2. Ga_3Si and As_3Si

The Ga_3Si signal [Fig. 2(c)], assumed to correspond to Si_{As} acceptors, exhibits pronounced maxima near the doped/undoped interfaces in the as-grown sample. On the undoped side, the profile forms a sharp front, while on the doped side, it decays gradually. Within the doped layer, Ga_3Si intensity decreases linearly with depth in the direction of the surface. Annealing enhances the Ga_3Si signal, with broader and smoother profiles observed between 800 and 950 °C. Diffusion-like tails extend into nominally undoped regions, though not as far as those of As_3Si [Fig. 2(d)]. At 1000 °C, the profile shows a distinct plateau and extended tail.

The As_3Si signal [Fig. 2(d)], which under our defect model represents a convolution of Si_{Ga} and $Si_{Ga}V_{Ga}$ contributions, displays uniform intensity across the doped layer in the as-grown sample. With annealing, it evolves into a broad plateau with increasing intensity up to 950 °C, followed by a decrease at 1000 °C.

These qualitative depth profiles provide valuable insights into the behavior and redistribution of silicon-related defects during annealing. However, they do not allow quantitative determination of individual defect concentrations, especially given the ambiguous nature of the As_3Si signal [Eq. (6)]. Moreover, the quantification framework applied in this study relies on a specific defect model tailored to nominal growth conditions, assuming a well-defined silicon defect landscape. However, under high-temperature annealing, especially in arsenic-deficient environments, the stability and formation energies of competing defect species may shift. Therefore, before proceeding to quantitative defect analysis, it is necessary to assess the arsenic distribution within the samples, as it may influence the applicability of the adopted defect model.

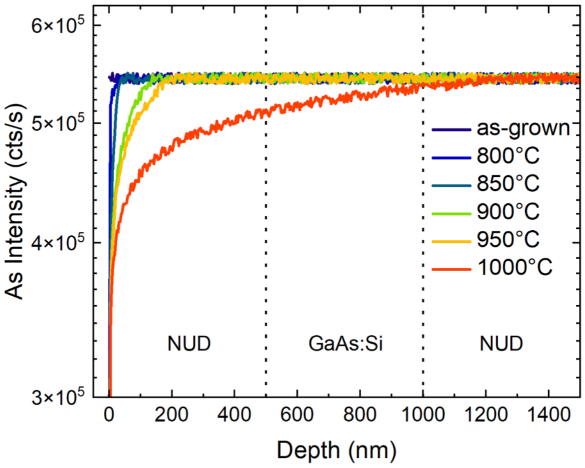

FIG. 3. Qualitative arsenic concentration distribution within GaAs/GaAs:Si/GaAs structures for as-grown and annealed samples. The arsenic profiles indicate a progressive escape of arsenic from the samples with increasing annealing temperature. Vertical lines indicate the borders between the nominally undoped (NUD) and Si-doped layers.

3. Arsenic distribution

Figure 3 presents the intensity depth profiles obtained for arsenic in all GaAs/GaAs:Si/GaAs samples, both as-grown and annealed.

At annealing temperatures below 1000 °C, arsenic depletion is confined to relatively shallow layers, with a maximum depth of approximately 200 nm at 950 °C. These regions lie outside the nominally doped region (500–1000 nm) and do not overlap with areas where diffused silicon-related species are observed. In contrast, at 1000 °C, significant arsenic escape occurs not only from the surface but also from the doped region itself. Despite the use of a GaAs cover to minimize arsenic loss, the results in Fig. 3 demonstrate that the protective mechanism was ineffective at this temperature.

B. Interpretation of qualitative profiles within the defect model framework

The qualitative ULIE-SIMS profiles (Fig. 2) suggest distinct redistribution behaviors for different silicon-related species during thermal annealing, and their interpretation can be analyzed within the framework of the adopted defect model and observed arsenic loss. The minimal change in the Si_2 intensity and shape indicates low diffusivity and high thermal stability of Si pairs. Notably, this stability persists even under arsenic-deficient conditions at 1000 °C, underscoring the chemical resilience of Si–Si pair configurations and their insensitivity to changes in the local arsenic environment.

In contrast to the relatively stable Si_2 signal, the Ga_3Si and As_3Si signals exhibit a more dynamic response to annealing. The enhancement of the Ga_3Si signal suggests increased Si incorporation on arsenic sites, while its confined spatial distribution and modestly evolving diffusion tails indicate rather low mobility of the Si_{As} defect. The As_3Si signal, reflecting a convolution of contributions from Si_{Ga} and $Si_{Ga}V_{Ga}$ defects, shows that a broader spatial extent relative to Ga_3Si and Si_2 suggests that Si_{Ga}-type defects are more mobile. The reduced As_3Si tail compared to total Si may reflect either lower mobility of Si_{Ga}-related defects or simply worse detection sensitivity for polyatomic signals. We favor the latter explanation, as ULIE-SIMS sensitivity to polyatomic ions is generally lower, leading to apparent profile truncation in low-concentration regions.

At 1000 °C, both Ga_3Si and As_3Si signals exhibit distinct changes. A plateau and extended tails emerge in the Ga_3Si profile, and a shift in the As_3Si intensity trend appears within the nominally doped region. These effects are likely linked to enhanced arsenic depletion in the doped layer under As-poor conditions at elevated temperatures.

It is important to recognize that a known consequence of such significant arsenic loss from a GaAs surface is the formation of Ga droplets, which creates considerable initial surface topography.[35–37] This roughness could potentially introduce measurement artifacts in SIMS, such as an apparent broadening of features, particularly at 1000 °C.

While surface roughness may influence apparent profile shapes, a further intrinsic limitation of SIMS and ULIE-SIMS needs to be considered. The sensitivity of SIMS to changes in the matrix element concentration is insufficient to detect variations in arsenic stoichiometry at a level that would be electronically significant. SIMS does not provide direct information on the vacancy distribution, and thus, the observed stability of the arsenic signal does not preclude changes in the arsenic vacancy (V_{As}) population within the material.

Nevertheless, the defect model adopted for this study assumes that complexes involving silicon atoms and arsenic vacancies, as well as isolated arsenic vacancies, do not exist at concentrations high enough to influence the net carrier concentration. This assumption is grounded in the established understanding of the defect landscape in highly n-doped GaAs:Si. The literature is largely in agreement that the $Si_{Ga}V_{Ga}$ complex is the dominant compensating defect in such materials. For example, Bondarenko *et al.* studied n-type samples with Si concentrations similar to those in our doped layer, annealed under a controlled arsenic vapor pressure, and identified $Si_{Ga}V_{Ga}$ as the key defect; V_{As} was found to be significant only in annealed undoped samples.[22] It can also be potentially expected to play a non-negligible role for samples with low dopant concentration.

The experimental configuration used in the present study was designed to create conditions analogous to arsenic-rich annealing for the critical buried layer. The Si-doped region was located 500 nm below the surface and was protected by both an undoped GaAs layer and an external GaAs piece. This multi-layer structure serves as a physical barrier to arsenic escape. Although the surface layer is sacrificially consumed, the buried doped layer is effectively protected, mimicking an anneal under As-rich conditions. Consequently, the application of a defect model appropriate for n-type GaAs:Si annealed under an As-rich environment is considered the most accurate approximation for the system investigated.

It is, however, acknowledged that the $Si_{Ga}V_{As}$ complex has been identified in previous studies of n-type GaAs, specifically in bulk crystals grown by the Bridgman method.[23,24] These observations were made under two distinct scenarios. The defect was found in highly Si-doped samples after a high-temperature anneal. Although this anneal was performed in an arsenic atmosphere, the conditions have been characterized as thermodynamically As-poor due to the low vapor pressure relative to the temperature, which is known to favor the formation of arsenic vacancies.[24] The defect was also identified in as-grown, unintentionally doped samples where the horizontal Bridgman growth method itself is known to produce Ga-rich (As-poor) stoichiometry.[24]

In contrast, the samples investigated in the present study differ in two fundamental aspects: the crystal growth technique and the annealing environment. First, MOVPE growth under As-rich conditions (i.e., high V/III ratio) is known to influence the native defect formation energetics in GaAs.[11,38] In contrast, bulk Bridgman-grown GaAs, typically obtained under comparatively As-poor conditions, exhibits a distinct defect landscape.[23,24] It is, therefore, reasonable to expect that the initial defect distribution in our MOVPE-grown layers differs from that in bulk Bridgman crystals. Second, our annealing procedure, which employs a protective cap, creates a localized As-rich environment for the buried layer. This condition suppresses the formation of arsenic vacancies, thereby preventing the formation of $Si_{Ga}V_{As}$.[11]

In light of the preceding analysis, the simplified defect model employed in this work, which excludes arsenic vacancy V_{As}-related species, is considered appropriate for describing the dominant defect behavior under the specific thermal and structural conditions investigated. However, it is essential to recognize that this model is not universally applicable. In particular, its relevance may be limited for the sample annealed at the highest temperature of 1000 °C. Under these conditions, more pronounced arsenic loss may facilitate the formation of V_{As}-related complexes or other defect species not captured within the current framework. Consequently, while the adopted model describes defect behavior across most of the studied temperature range, interpretation of results for the 1000 °C case must be approached with caution, as deviations from the assumed defect landscape could compromise derived defect concentrations.

Building on the adopted framework and the insights gained from the qualitative depth profiles, Sec. IV C develops a quantitative approach for correlating ULIE-SIMS signal intensities with carrier concentration, which is a step toward reconstructing individual defect distributions.

C. ULIE-SIMS carrier concentration measurement

1. Empirical calibration model

GaAs:Si exhibits significant compensation from Si-based defects, requiring a complex carrier concentration calibration approach based on a combination of As_3Si and Ga_3Si signals reflecting the influence of all charged defects: Si^{+}_{Ga}, $Si_{Ga}V^{2-}_{Ga}$, and Si^{-}_{As}. Based on comparison of ECV carrier concentration distributions with the measured ULIE-SIMS depth profiles of As_3Si and Ga_3Si, we tested and validated the hypothesis that the carrier concentration profile for GaAs:Si can be expressed as a linear combination of the As_3Si and Ga_3Si ULIE-SIMS signals,

$$n^{\text{ULIE-SIMS}} = \alpha \text{As}_3\text{Si} - \beta \text{Ga}_3\text{Si}, \tag{7}$$

where $n^{\text{ULIE-SIMS}}$ is the carrier concentration derived from the ULIE-SIMS signals, and α and β are proportionality factors representing the contributions of the As_3Si and Ga_3Si signals, respectively.

Figure 4 illustrates the basis for the hypothesis by showing the key relationship between the ULIE-SIMS signals and the carrier concentration described in Eq. (7). In Fig. 4, the ECV carrier concentration profile (left y axis) is overlaid with the raw ULIE-SIMS signals for As_3Si and Ga_3Si (right y axis), plotted on the same depth scale for the as-grown GaAs/GaAs:Si/GaAs structure. This comparison visually supports the linear combination relationship between carrier concentration and As_3Si and Ga_3Si signals.

Although the initial validation of our hypothesis was carried out using the as-grown GaAs/GaAs:Si/GaAs structure, optimal values of the parameters α and β were determined using sets of non-annealed calibration samples with a simple structure, in which the nominally doped layer was located directly at the sample surface. These reference samples exhibited superior surface quality, confirmed by optical microscopy to be "mirror-like" and defect-free. Furthermore, the inclusion of calibration sample sets also enabled evaluation of the universality of parameters α and β, providing an additional rationale for their use in the optimization procedure.

The first calibration set (C1–C3) was used to optimize α and β, which reflect the relative contributions of the As_3Si and Ga_3Si signals to the carrier concentration. The final values, along with their uncertainties estimated from a sensitivity analysis involving an independent sample set (C4-C6) and the intrinsic variability of polyatomic SIMS signals, were $\alpha = (6.78 \pm 0.16) \times 10^{15}$ cm^{-3}s/cts and $\beta = (9.64 \pm 0.30) \times 10^{15}$ cm^{-3}s/cts. For more details on the calibration procedure and error estimation, see the "Calibration procedure" and "Error estimation" sections in the supplementary material.

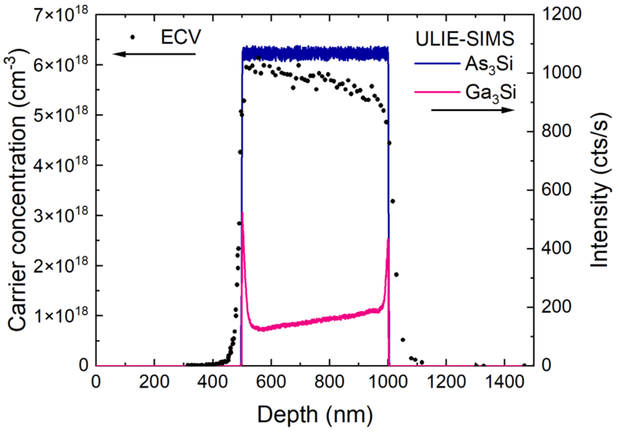

FIG. 4. Carrier concentration profile measured by ECV profiling (left y axis), overlaid with raw ULIE-SIMS signals of As_3Si and Ga_3Si (right y axis) for the as-grown GaAs/GaAs:Si/GaAs structure. The comparison illustrates the correlation between the carrier concentration and the differential behavior of the two polyatomic ULIE-SIMS signals [Eq. (7)].

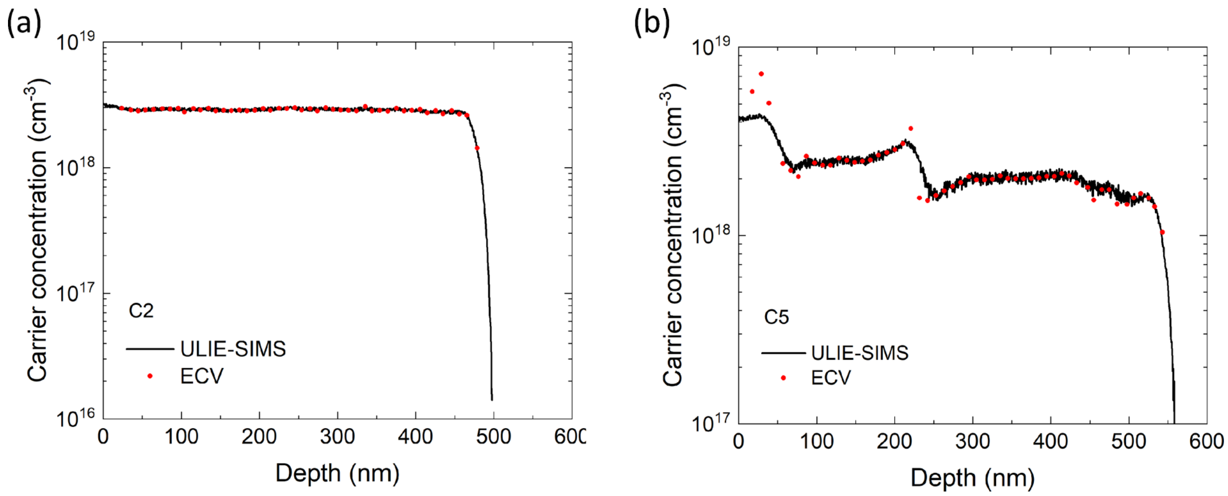

FIG. 5. Comparison of the carrier concentration distribution measured using the ECV technique with the distribution obtained from Eq. (7) using ULIE-SIMS depth profiles of As_3Si and Ga_3Si signals for (a) a C2 (medium-doped: a total Si level of 4.25×10^{18} atoms/cm^3, 1st batch) calibration sample and (b) a C5 [2nd batch, intentional substrate misorientation 0.2° toward (111)A; a total Si level of 7.2×10^{18} atoms/cm^3] calibration sample.

Figure 5(a) shows the carrier concentration distribution for the medium-doped calibration sample (C2), comparing ECV measurements with profiles derived using the calibrated ULIE-SIMS signals. Analogous results for the remaining calibration samples, C1 (low doped) and C3 (highly doped) are provided in Figs. S1(a) and S1(b) of the supplementary material. The two methods exhibit very good agreement for all samples considered.

An independent second set of samples (C4–C6) was used for two key purposes. First, to evaluate the predictive accuracy of the model, specifically in the case of non-uniform carrier concentration profiles and second, to estimate the uncertainty of α and β through sensitivity analysis, which evaluated how the fitted values would vary if a different combination of calibration samples were used (see "Error estimation" in the supplementary material). Figure 5(b) presents the carrier concentration distribution for sample C5, comparing ECV and ULIE-SIMS-derived profiles. Results for C4 and C6 are available in Figs. S2(a) and S2 (b) of the supplementary material. The relative deviations between the integrals of the ULIE-SIMS-derived and ECV carrier concentration profiles were found to not exceed 3.93%, confirming the high accuracy and transferability of the calibrated coefficients.

Beyond validating the model, this comparison highlights key strength of ULIE-SIMS: its superior depth resolution enables accurate profiling in regions of steep concentration gradients. For instance, in Fig. 5(b), ULIE-SIMS better resolves carrier transitions near 50 and 220 nm, where ECV resolution is limited.

The empirical relationship expressed in Eq. (7), derived directly from the data presented in this work, serves as the foundation for further quantification and interpretation of ULIE-SIMS results in the context of Si-based defects in GaAs. While Eq. (7) successfully captures the carrier concentration distribution, it is important to recognize its inherent limitations. In particular, although the Ga_3Si signal is assumed to scale with the Si_{As} concentration [Eq. (4)], the associated proportionality constant remains unknown as discussed in more detail in the "Limits of applicability and interpretative challenges in ULIE-SIMS carrier concentration analysis" section of the supplementary material. Similarly, the As_3Si signal, reflecting contributions from both Si_{Ga} and $Si_{Ga}V_{Ga}$, is governed by an unknown functional relationship with the respective defect concentrations [Eq. (6)]. As a result, Eq. (7) enables robust estimation of carrier concentration but does not permit direct decomposition of the signal into individual defect contributions.

2. Application to GaAs/GaAs:Si/GaAs structures

Using the empirically confirmed relationship [Eq. (7)], ULIE-SIMS enables quantitative reconstruction of carrier concentration profiles from As_3Si and Ga_3Si signals.

Accurate ECV profiling of the annealed GaAs/GaAs:Si/GaAs samples presented significant challenges, primarily due to surface degradation arising from arsenic depletion (Fig. 3). This degradation introduced substantial surface roughness and inhomogeneities, compromising the reliability of carrier concentration measurements,[33,34,39] specifically influencing the depth scale.

Figure 6 presents the comparison of ULIE-SIMS and ECV carrier concentration profiles obtained for GaAs/GaAs:Si/GaAs structures in the as-grown state and following annealing at 800–1000 °C. The ECV results presented here are depth-corrected to the ULIE-SIMS result. A full discussion of ECV accuracy and measurement procedures is provided in the "ECV measurements" section of the supplementary material.

The ULIE-SIMS and ECV results show very good overall agreement across all annealing conditions. Notably, this agreement persists even for the sample annealed at 1000 °C—despite the fact

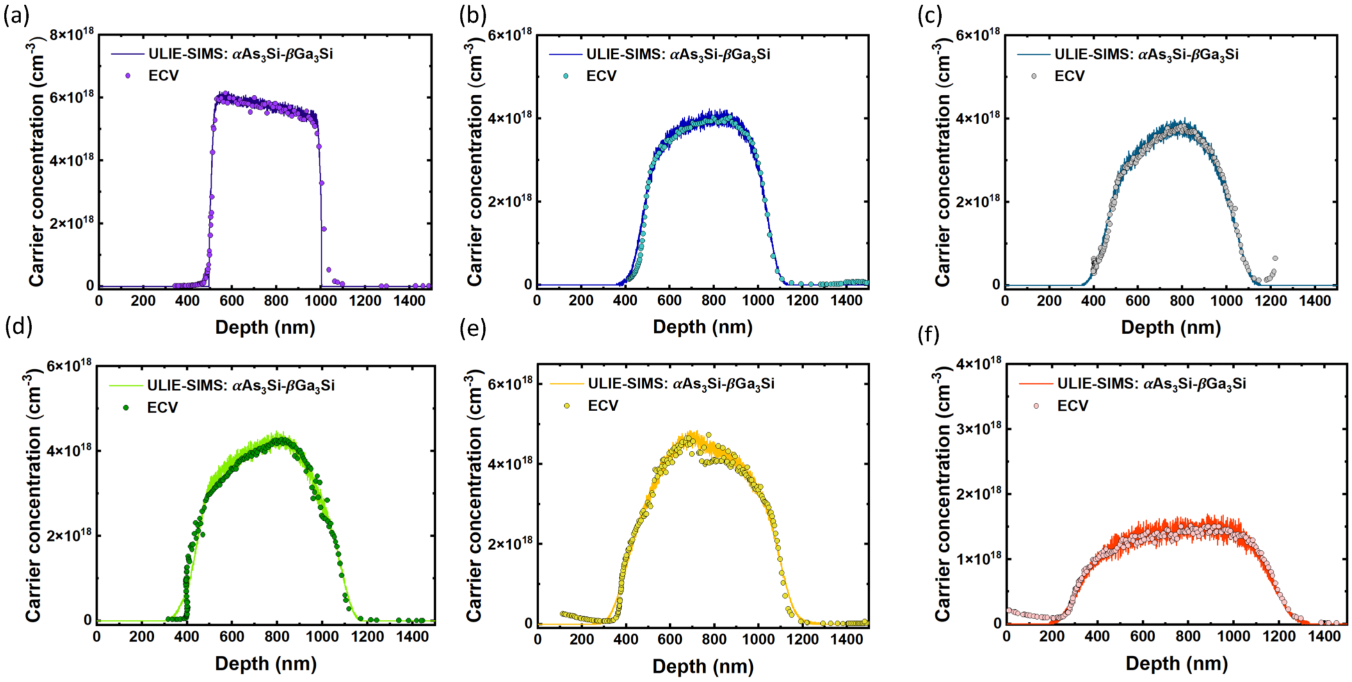

FIG. 6. Carrier concentration profiles obtained from ULIE-SIMS using Eq. (7) with calibrated α and β, compared with depth-aligned ECV profiles for GaAs/GaAs:Si/GaAs samples in the (a) as-grown state and after annealing at (b) 800, (c) 850, (d) 900, (e) 950, and (f) 1000 °C. ULIE-SIMS and ECV profiles show high consistency across all samples, confirming the reliability of the ULIE-SIMS approach for quantitative carrier concentration profiling.

that this case may fall outside the assumed defect model due to the arsenic-deficient environment, which could promote the formation of V_{As}-related defects not explicitly included in the model.[23,24]

This is also a critical observation, considering the potential for topography-induced artifacts in SIMS. For the calibrated linear combination of Ga_3Si and As_3Si to accurately reproduce the carrier concentration measured by ECV, these polyatomic signals must retain physically meaningful, quantitative information about the charged-defect landscape, rather than reflecting topographical noise. This result strongly suggests that any impact from initial surface roughness on the measurement of the buried layer is minimal. It validates the use of this method for quantitative carrier concentration analysis even under challenging annealing conditions where traditional techniques may be compromised.

The as-grown sample exhibits the highest carrier concentration in the doped layer (between ∼5 and $6 \times 10^{18}\,\mathrm{cm}^{-3}$), indicating superior electrical properties compared to annealed samples. However, even in the as-grown material, the ratio of carrier concentration to total Si content (1.4×10^{19} atoms/cm^3) is only about 40%, implying that a substantial fraction of the incorporated silicon remains compensated. While this ratio provides useful information, it does not fully capture the nuanced interplay of various compensation processes. Consequently, further defect-specific analysis is required to unravel the distinct contributions of individual compensation mechanisms.

Carrier concentration profiles for samples annealed at temperatures between 800 and 950 °C demonstrate a significant initial reduction compared to the as-grown state; however, differences among these temperatures remain moderate, resulting in carrier concentrations consistently in the range of ∼3–$4 \times 10^{18}\,\mathrm{cm}^{-3}$. In contrast, the sample annealed at 1000 °C displays a pronounced reduction in carrier concentration (below ∼$2 \times 10^{18}\,\mathrm{cm}^{-3}$). This marked decline coincides with the pronounced escape of arsenic (Fig. 3) at this elevated annealing temperature.

Building on these carrier concentration results, Sec. IV D leverages the established calibration framework to reconstruct depth-resolved concentration profiles of individual silicon-related defect species.

D. Defect quantification framework

1. Derivation of quantitative model equations

The quantitative analysis of Si-based defect species is grounded in the calibrated ULIE-SIMS signals corresponding to distinct polyatomic ions. The Si_2 signal is associated with Si_p (Si_{Ga}–Si_{As} pairs), while Ga_3Si serves as an indicator of Si_{As}. These signals, combined with the total Si concentration ([Si]) and the net carrier concentration (n) derived from ULIE-SIMS, allow

TABLE I. Values of calibration parameters for all measured ULIE-SIMS signals and corresponding physical quantities.

ULIE-SIMS signal (cts/s)	Calibration parameter (cm^{-3}s/cts)	Physical interpretation
Si	$h = (1.246 \pm 0.019) \times 10^{15}$	[Si] = hSi; total Si concentration
Si_2	$h_1 = (6.61 \pm 0.28) \times 10^{14}$	$[Si_p] = h_1 Si$; Si_p concentration
As_3Si	$\alpha = (6.78 \pm 0.16) \times 10^{15}$	
Ga_3Si	$\beta = (9.64 \pm 0.30) \times 10^{15}$	$n = \alpha As_3Si - \beta Ga_3Si$; carrier concentration
Ga_3Si	$\beta_1^{max} = 2.05 \times 10^{15}$(estimate)	$[Si_{As}] = \beta_1 Ga_3Si$; Si_{As} concentration

for quantitative defect reconstruction despite the ambiguous interpretation of the As_3Si signal.

From Eqs. (1) and (2), we derive the following expressions for the concentrations of $Si_{Ga}V_{Ga}$ and Si_{Ga}:

$$[Si_{Ga}V_{Ga}] = \frac{[Si] - n - 2[Si_{As}] - 2[Si_p]}{3}, \tag{8}$$

$$[Si_{Ga}] = \frac{2[Si] + n - [Si_{As}] - 4[Si_p]}{3}. \tag{9}$$

To express Eqs. (8) and (9) in terms of experimentally measured ULIE-SIMS profiles, we apply the assumption from Eq. (4). Based on this relationship, another calibration parameter is introduced: β_1, which converts the Ga_3Si signal intensity into Si_{As} concentration; thus, we define

$$[Si_{As}] = \beta_1 Ga_3Si. \tag{10}$$

It is important to distinguish β_1 from the previously introduced β coefficient. Although both relate to the Ga_3Si signal, β should not be interpreted as a direct calibration factor for $[Si_{As}]$. The empirical relationship expressed in Eq. (7), derived directly from experimental data, serves as the foundation for carrier concentration estimation. However, there is no direct evidence that the β coefficient used in this context can also be interpreted as a quantitative calibration factor for Ga_3Si in relation to Si_{As} concentration. In fact, analysis presented in the "Limits of applicability and interpretative challenges in ULIE-SIMS carrier concentration analysis" section of the supplementary material provides evidence that such an interpretation may not be valid. To complete the formulation, we also express the total silicon concentration and the Si_p concentration in terms of their respective ULIE-SIMS signals. These are calibrated using previously established coefficients h and h_1, respectively,

$$[Si] = hSi, \tag{11}$$

$$[Si_p] = h_1 Si_2. \tag{12}$$

By substituting Eqs. (7) and (10)–(12) into the expressions for $[Si_{Ga}V_{Ga}]$ and $[Si_{Ga}]$ [Eqs. (8) and (9)], we derive the final formulas linking these defect concentrations directly to measurable ULIE-SIMS signals,

$$[Si_{Ga}V_{Ga}] = \frac{hSi - \alpha As_3Si + \beta Ga_3Si - 2\beta_1 Ga_3Si - 2h_1 Si_2}{3}, \tag{13}$$

$$[Si_{Ga}] = \frac{2hSi + \alpha As_3Si - \beta Ga_3Si - \beta_1 Ga_3Si - 4h_1 Si_2}{3}. \tag{14}$$

These expressions contain a single remaining unknown calibration parameter, β_1, whereas all other parameters have been previously determined and are summarized in Table I. Their values were obtained using a combination of calibration strategies, including standard SIMS with reference samples for h, extrapolation from the empirically stable Si_2/Si signal ratio across multiple Si-based materials to derive h_1, and comparative fitting to ECV-derived carrier concentration profiles for α and β. Consequently, determining β_1 enables the complete reconstruction of depth-resolved concentration profiles for all considered Si-related defects using ULIE-SIMS data alone.

2. Calibration of Si_{As}

To estimate β_1, we imposed the condition that calculated from Eq. (13) $[Si_{Ga}V_{Ga}]$ remains non-negative across all depths where As_3Si, Ga_3Si, and total Si signals exceed detection thresholds and fall within validated intensity ranges. The maximum value ensuring this condition, β_1^{max}, was found to be approximately 2.05×10^{15} cm^{-3}s/cts. This estimation was performed using the as-grown sample, as its measured signals impose the most restrictive upper limit on β_1. In annealed samples, the same physical constraint could be satisfied with even larger β_1 values, so using the as-grown case ensures that the chosen β_1^{max} is the most conservative value supported by our data. In the absence of reference material with the known $[Si_{As}]$, this physically constrained approach provides the most direct and experimentally justified means to bound β_1. As the lower boundary for β_1, we adopted the calibration factor corresponding to the detection limit for total silicon (h), justified by the typically worse detection limit observed for polyatomic signals compared to monatomic Si. This sets a relatively narrow range of plausible β_1 parameter values (from more than 1.24 to 2.05×10^{15} cm^{-3}s/cts) and implies only a minor contribution of Si_{As} to the overall silicon concentration. Specifically, in the as-grown sample, Si_{As} constitutes up to roughly 14% of the total silicon at the interfaces between doped and undoped layers and only slightly above 2% deep within the doped region. Consequently, given such low Si_{As} concentrations and the limited calibration range for β_1, even an overestimation of this parameter will have a relatively small impact on the calculated concentrations of $Si_{Ga}V_{Ga}$ and Si_{Ga} [Eqs. (13) and (14)] within the nominally doped layer. Considering that the lower boundary of the β_1 range corresponds to negligible Si_{As} content, we adopted the upper boundary (β_1^{max}) as the calibration coefficient for the Ga_3Si signal to obtain a quantitative estimate of the Si_{As} defect concentration.

E. Quantitative depth profiles of Si-based defects

Figure 7 presents calibrated depth profiles of total Si and all considered silicon-based defects, namely, Si_p, Si_{As}, Si_{Ga}, and $Si_{Ga}V_{Ga}$, obtained for the as-grown GaAs/GaAs:Si/GaAs structure as well as for samples annealed at temperatures ranging from 800 to 1000 °C. These profiles were determined within an adopted

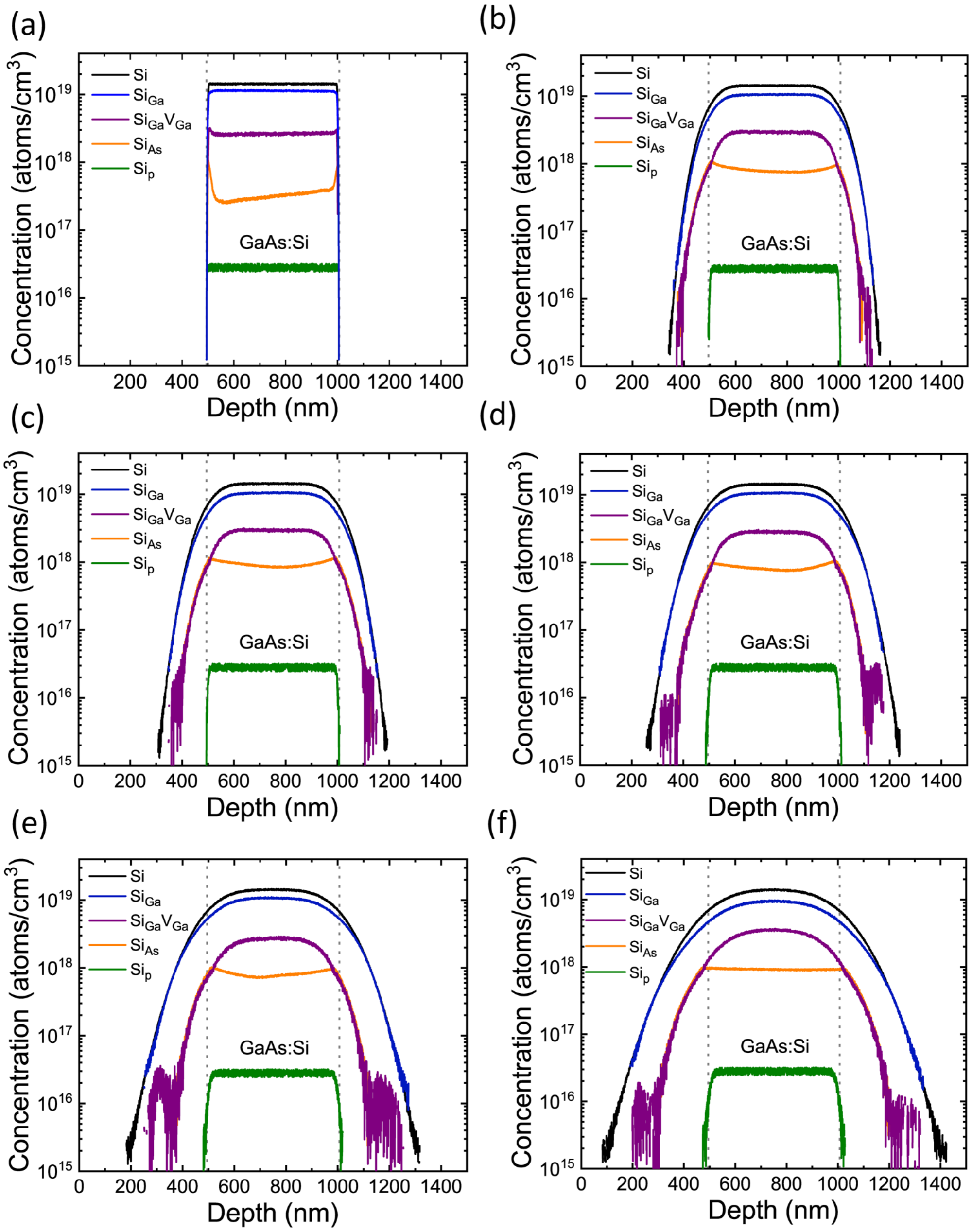

FIG. 7. Quantitative depth profiles of Si-based defects Si_{Ga}, $Si_{Ga}V_{Ga}$, Si_{As}, Si_p, and total Si obtained for a GaAs/GaAs:Si/GaAs sample in (a) the as-grown state and after annealing at (b) 800, (c) 850, (d) 900, (e) 950, and (f) 1000 °C. The depth profiles of individual defects were calculated based on Eqs. (10)–(14) using calibration parameters summarized in Table I.

model framework using Eqs. (10)–(14) and the calibration coefficients summarized in Table I. While all temperatures are analyzed consistently within this framework, the 1000 °C sample exhibited substantial arsenic loss (Fig. 3), which may promote the formation of additional defect species not included in the model. The implications of this potential deviation are addressed in Sec. V.

1. Defect distributions in the as-grown sample: Bulk vs interface regions

The analysis first focuses on the nominally doped region of the as-grown sample [Fig. 7(a)], excluding the ∼30 nm interfacial zones on either side of the doped layer, located between approximately 500 and 1000 nm. In the considered region, atoms predominantly occupy gallium sites ($\mathrm{Si_{Ga}}$ and $\mathrm{Si_{Ga}V_{Ga}}$), comprising approximately 96.8%–97.8% of the total silicon in the doped region. The $\mathrm{Si_{Ga}}$ donors exhibit a slight increase in concentration moving from the substrate toward the surface, reaching an average concentration of about $1.13 \times 10^{19}\,\mathrm{cm^{-3}}$, corresponding to roughly 79.0% of the total silicon. The compensating acceptor-like $\mathrm{Si_{Ga}V_{Ga}^{2-}}$ complexes, formed by gallium atoms paired with a Ga vacancy, play a dominant role in limiting carrier concentration. These complexes have an average concentration of about $2.64 \times 10^{18}\,\mathrm{cm^{-3}}$ (18.4% of [Si]), effectively neutralizing twice as many donors. The influence of silicon occupying arsenic lattice sites ($\mathrm{Si_{As}}$) is negligible within the bulk of the doped layer, with an average $\mathrm{Si_{As}/Si_{Ga}}$ ratio of approximately 0.0278. Notably, this ratio exhibits a slight gradient, decreasing approximately linearly along the growth direction, with values ranging from 0.033 to 0.0238. The compensating effect due to silicon pairs is even less significant, averaging about $1.25 \times 10^{16}\,\mathrm{cm^{-3}}$ (0.4% of total silicon), thus minimally impacting effective carrier concentration.

Figure 7(a) reveals a distinctly different behavior at the interfaces with the nominally undoped layers, where local maxima in the concentrations of $\mathrm{Si_{Ga}V_{Ga}}$ and $\mathrm{Si_{As}}$ are observed. Figure 8 presents a close-up to the defect-to-total Si ratio at the interface closest to the substrate area. This interface exhibits a narrow region (∼4.5 nm, highlighted in yellow in Fig. 8), with $\mathrm{Si_{Ga}}$ concentration dropping to about 73% of total [Si] at its minimum while $\mathrm{Si_{As}}$ rises to a local maximum of 14.85% of total [Si] and $\mathrm{Si_{Ga}V_{Ga}}$ peaks at approximately 21.1% of total [Si]. Beyond this abrupt interface, the defect concentrations gradually stabilize over ∼15 nm (green background in Fig. 8), converging toward the average concentration characteristic of the doped bulk region.

At the second interface closer to the surface, a similar but slightly broader characteristic region of gradual stabilization is observed (∼25 nm), as well as more pronounced maxima for $\mathrm{Si_{Ga}V_{Ga}}$ (up to 22.8% of Si total) and for $\mathrm{Si_{As}}$ (up to 12.44% of Si total), alongside a deeper minimum for $\mathrm{Si_{Ga}}$ (∼70.5% of Si total). Nevertheless, the rapid change remains comparable (∼4.5 nm) to that of the buried interface.

2. Annealed induced changes

To gain deeper insight into the thermally induced redistribution mechanisms of silicon-based defects, we analyzed the evolution of $\mathrm{Si_{Ga}}$, $\mathrm{Si_{Ga}V_{Ga}}$, $\mathrm{Si_{As}}$, and $\mathrm{Si_p}$ depth profiles in GaAs:Si structures subjected to post-growth annealing at temperatures between 800 and 1000 °C. Figures 9(a)–9(d) present a comparative visualization of these defects, with each panel illustrating the temperature-dependent behavior of a specific species: $\mathrm{Si_p}$ (a), $\mathrm{Si_{As}}$ (b), $\mathrm{Si_{Ga}}$ (c), and $\mathrm{Si_{Ga}V_{Ga}}$ (d). This enables a direct assessment of changes in both concentration and spatial distribution, allowing for a precise identification of thermally induced transformations and insights into the underlying physical processes.

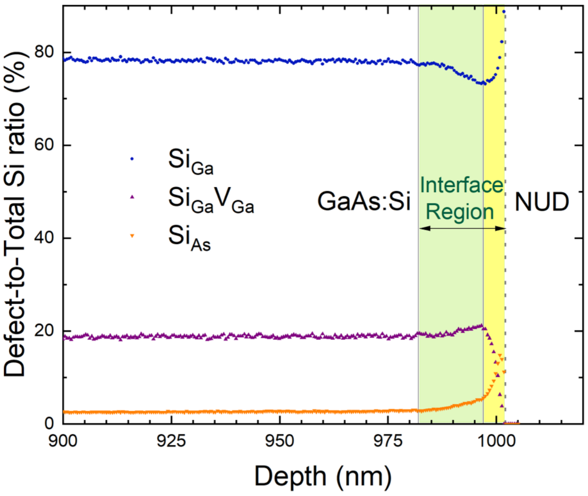

FIG. 8. Close-up view of the defect-to-total Si ratio distribution for an as-grown GaAs/GaAs:Si/GaAs structure at the interface between the nominally undoped GaAs layer and the doped GaAs:Si layer [corresponding to the deeper buried interface in Fig. 7(a)]. The yellow shaded region (∼4.5 nm) marks the abrupt interface zone, characterized by sharp changes in defect-to-total Si ratios. The green-shaded region (∼15 nm) indicates the subsequent transition zone, where defect concentrations gradually stabilize toward defect-to-total Si ratio values representative of the doped bulk region.

a. Si_p (Si pairs). The concentration of $\mathrm{Si_p}$ remains nearly constant across the entire range of annealing temperatures [Fig. 9(a)]. However, the temperature-dependent broadening of the depth profiles provides clear evidence of thermally activated diffusion of $\mathrm{Si_p}$, even though the overall extent of migration remains relatively limited. To quantify this behavior, diffusion coefficients were extracted by fitting the analytical solution of the one-dimensional diffusion equation to the experimental $\mathrm{Si_p}$ profiles. These values were then plotted in Arrhenius coordinates, and a linear fit was performed to determine the activation energy (E_a) and pre-exponential factor (D_0), yielding $E_a = (1.6 \pm 0.1)\,\mathrm{eV}$ and $D_0 = 1.53 \times 10^{-9}\,\mathrm{cm^2/s}$. Full details of the diffusion model and fitting procedure are provided in the "Diffusion" section of the supplementary material. The Arrhenius plot obtained for the Si pair defect is shown in Fig. 10(a).

b. Si_{As}. The concentration of $\mathrm{Si_{As}}$ increases after annealing at all investigated temperatures [Fig. 9(b)]. The $\mathrm{Si_{As}/Si_{Ga}}$ ratio varies across the doping profile, reaching minimum values in the central region of the nominally doped layer and maximum values near the interfaces. For samples annealed at 800–950 °C, the central ratio falls within the range of 0.065–0.076. The highest central ratio observed in this study, 0.092, corresponds to the sample annealed at 1000 °C, which also exhibited arsenic depletion. For all annealed samples except the one treated at 1000 °C, the interfacial maxima of the Si_{As}/Si_{Ga} ratio lie between 0.15 and 0.21. In the 1000 °C sample, this maximum reaches 0.25. Although the total amount of Si_{As} within the nominally doped layer increases after annealing, the dependence on temperature is non-monotonic. The integrated Si_{As} dose in this region rises by a factor of 2.40 to 2.74 relative to the as-grown state. The largest increase (2.74×) occurs for the sample annealed at 850 °C, followed closely by the 1000 °C sample, which shows a 2.68× increase. Despite similar integrated concentrations, the Si_{As} depth profiles differ substantially between these two samples. In the 1000 °C sample, the profile is noticeably flatter and extends beyond the nominally doped region, in contrast to the less uniform and more confined distributions observed at lower annealing temperatures.

c. Si

c. Si_{Ga}. The concentration profile of Si_{Ga} exhibits behavior close to thermally activated diffusion from an initial uniform distribution [Fig. 9(c)]. Post-annealing, a general decrease in concentration is observed within the nominally doped region, accompanied by the development of diffusion-like tails extending toward both interfaces. However, the central part of the profile deviates from a simple Fickian diffusion model. In a purely diffusion-driven process, one would expect a monotonic decrease in concentration across the entire profile with an increasing temperature. To assess deviations from ideal diffusion behavior, the relative Si_{Ga} dose was quantified as a function of annealing temperature and normalized to the as-grown value [Fig. 10(b)]. Two regions were considered: the entire nominally doped layer (500–1000 nm) and the central

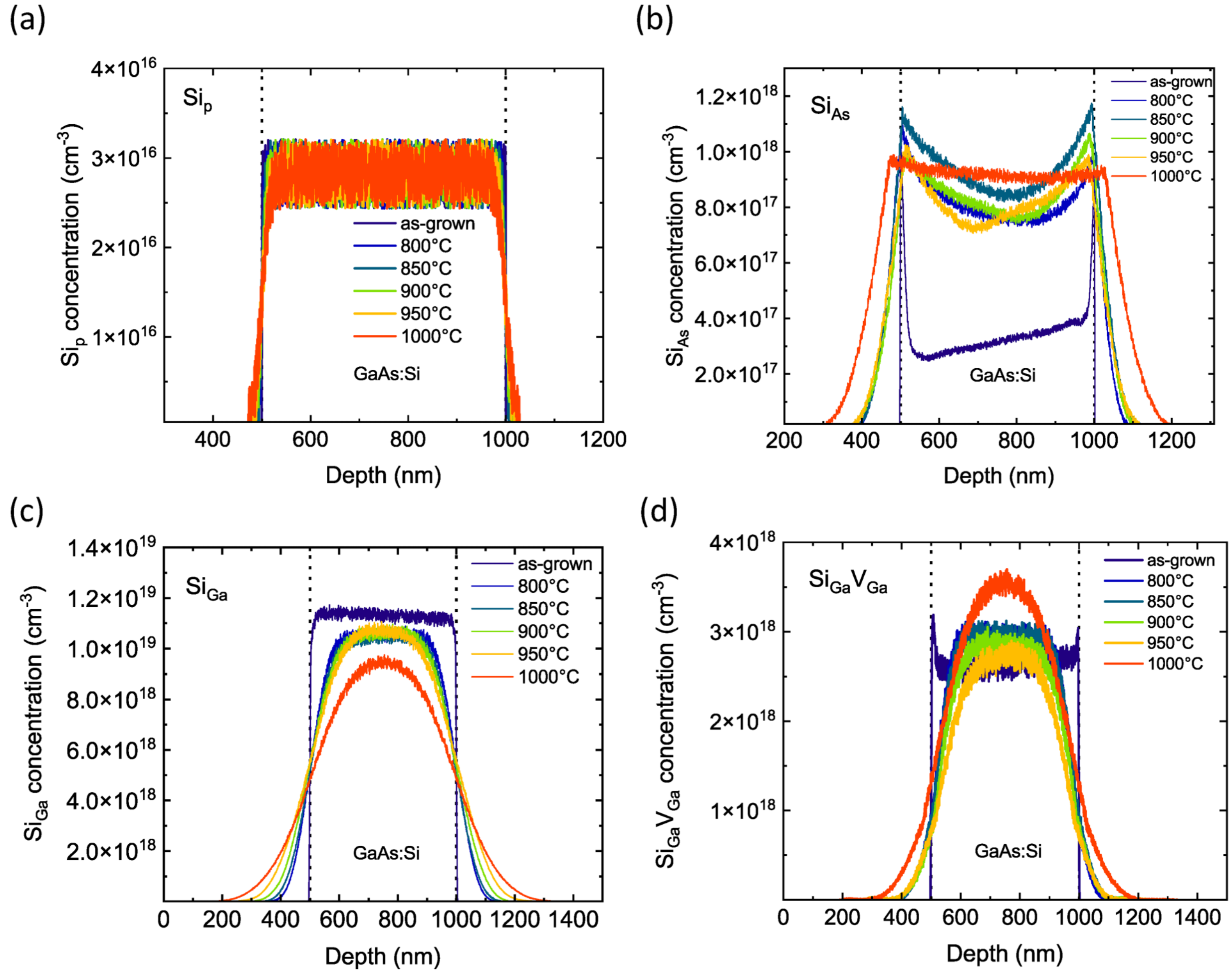

FIG. 9. Post-annealing depth profiles of silicon-based defects in GaAs:Si structures. Panels (a)–(d) show the temperature-dependent evolution of individual defect species: (a) Si_p, (b) Si_{As}, (c) Si_{Ga}, and (d) $Si_{Ga}V_{Ga}$ for samples annealed at temperatures ranging from 800 to 1000 °C. Each panel presents calibrated depth profiles, enabling a direct comparison of both concentration levels and spatial distributions across the annealing series.

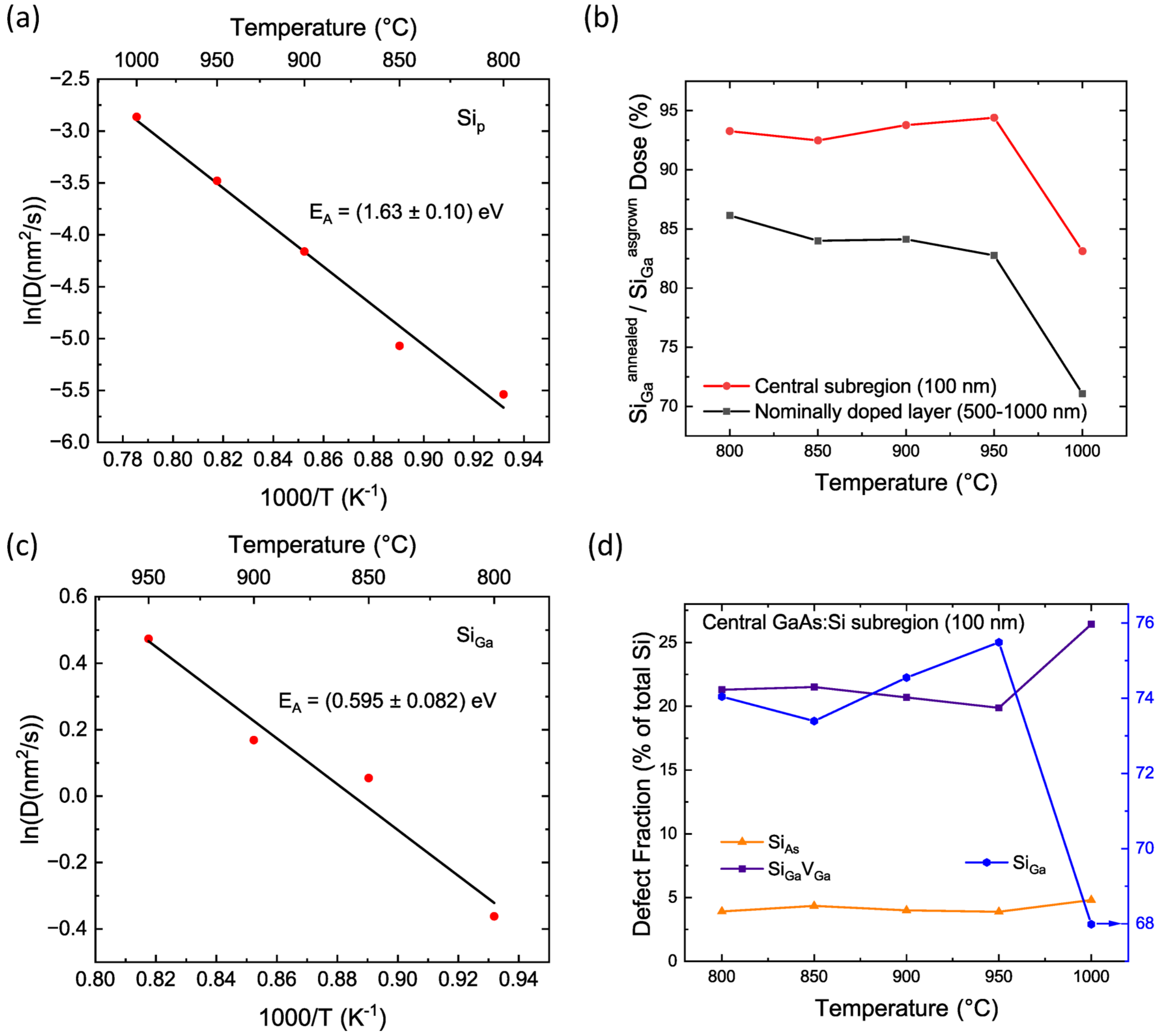

FIG. 10. Arrhenius plots and relative dose evolution of silicon-based defects in GaAs:Si as a function of annealing temperature. (a) Arrhenius plot for Si_p diffusion, derived from depth profiles. (b) Relative Si_{Ga} dose normalized to the as-grown value, shown for both the entire nominally doped region (500–1000 nm) and the central 100 nm subregion. The contrasting trends highlight the interplay between diffusion-driven depletion and the defect redistribution via site exchange mechanisms. (c) Arrhenius plot for Si_{Ga} diffusion, obtained using the slab approximation applied to the nominally doped region (excluding 1000 °C). (d) Evolution of Si-based defect fractions in GaAs:Si as a function of annealing temperature. The graph displays the percentage of total silicon incorporated as Si_{Ga}, $Si_{Ga}V_{Ga}$, and Si_{As} within the central 100 nm of the nominally doped region. Si_{Ga} data are shown on the right y axis.

100 nm zone centered at 750 nm. For the central region, a slight increase in the relative Si_{Ga} dose is observed between 850 and 950 °C, rising from approximately 92.5% to 94.4% of the as-grown value. In contrast, when integrating over the full nominally doped region, the Si_{Ga} dose decreases with increasing temperature. The only exception is the 900 °C sample, which exhibits a slight increase when compared to lower annealing temperature. At 1000 °C, a pronounced drop is observed in both regions, with the total Si_{Ga} dose decreasing to approximately 71% of the as-grown value in the entire nominally doped layer, and to about 83% in the central region.

To estimate the diffusivity of Si_{Ga}, diffusion coefficients were extracted by fitting the analytical solution of the one-dimensional diffusion equation to the concentration profiles within the nominally doped region, assuming constant initial concentration and idealized slab-like geometry. While this simplified model does not account for additional mechanisms, such as the observed increase in concentration, it provides a reasonable approximation of thermally activated diffusion. The sample annealed at 1000 °C was excluded from this analysis, as arsenic loss at this temperature alters the considered defect landscape and may introduce non-comparable conditions that could bias the extracted parameters. The resulting diffusion coefficients for the remaining temperatures were plotted in Arrhenius coordinates, yielding an approximately linear relationship. From the linear fit, an activation energy of $E_a = (0.595 \pm 0.082)$ eV and a pre-exponential factor of $D_0 = 4.5 \times 10^{-12}$ cm^2/s were obtained [Fig. 10(c)].

d. $Si_{Ga}V_{Ga}$. The evolution of an $\mathrm{Si_{Ga}V_{Ga}}$ distribution with annealing temperature is shown in Fig. 9(d). At 800 °C, an increase in the $\mathrm{Si_{Ga}V_{Ga}}$ concentration is observed in the central region of the nominally doped layer, accompanied by a reduction near the interfaces compared to the as-grown sample. Within the central zone, the fraction of $\mathrm{Si_{Ga}V_{Ga}}$ relative to the total Si content increases from approximately 18.3% (as-grown) to 20.5% and remains nearly unchanged at 850 °C (20.6%). With a further temperature increase, this fraction gradually decreases, reaching 19.8% at 900 °C and 19.0% at 950 °C. At 1000 °C, however, a marked increase is observed: the $\mathrm{Si_{Ga}V_{Ga}}$ fraction in the central region rises to 25.4%, exceeding all values registered at lower annealing temperatures. Additionally, a distinct change in the slope of the $\mathrm{Si_{Ga}V_{Ga}}$ diffusion tail appears beyond the $\mathrm{Ga_3Si}$ signal maxima, near the interfaces with the nominally undoped region.

Figure 10(d) presents the temperature dependence of the relative fraction of Si incorporated in the form of $\mathrm{Si_{Ga}}$, $\mathrm{Si_{Ga}V_{Ga}}$, and $\mathrm{Si_{As}}$ within the central 100 nm subregion of the nominally doped layer. By focusing on this central zone-where depth-dependent diffusion effects are minimized—the analysis emphasizes the intrinsic response of defect populations to annealing conditions.

V. DISCUSSION

A. Interpretation of quantitative defect profiles

1. Defect distribution in an as-grown sample

The quantitative depth profiles of Si-based defects provide a detailed view of dopant incorporation and their thermal redistribution in GaAs. The as-grown bulk region is dominated by silicon on the gallium sublattice, with only a minimal fraction of silicon atoms incorporating as $\mathrm{Si_{As}}$ acceptors. The $\mathrm{Si_{As}/Si_{Ga}}$ ratio agrees well with the average value of 0.027[18] reported by Ishida *et al.* for an epitaxial layer doped on a similar level grown by molecular beam epitaxy (MBE), indicating a strong resemblance in the defect landscape of epitaxial samples prepared by different methods. The Si-based defects' behavior at the interfaces becomes significantly more intricate, defined by the appearance of sharp, localized maxima in the concentrations of the compensating $\mathrm{Si_{Ga}V_{Ga}}$ and $\mathrm{Si_{As}}$. The observed defect distribution features at the interfaces between nominally doped and undoped layers can be interpreted through step-by-step physical reasoning based on transient changes in doping conditions during epitaxial growth. Initially, the undoped layer exhibits defect populations that are characteristic of As-rich optimized MOVPE growth conditions. These include arsenic antisites $\mathrm{As_{Ga}}$ gallium vacancies $\mathrm{V_{Ga}}$, and, to a lesser extent, arsenic vacancies $\mathrm{V_{As}}$.[40–44] The free electron concentration remains relatively low, establishing a baseline for the subsequent introduction of silicon dopants. Upon activating the silicon source, a significant influx of silicon atoms preferentially incorporates into gallium lattice sites ($\mathrm{Si_{Ga}}$), introducing donor states and increasing local electron concentration.[2,5,7,45] This transition modifies the local chemical potential and the Fermi level position[4,46,47] toward the conduction band, thereby altering the thermodynamic driving forces for defect formation. Silicon atoms start occupying arsenic sites ($\mathrm{Si_{As}}$) to accommodate for a sudden change by shifting the Fermi level back toward a valence band and closer to its position within an undoped layer, thus contributing to compensation. This behavior is consistent with the well-known amphoteric nature of silicon in GaAs.[2,6] Additionally, increased electron concentration reduces the formation energy for negatively charged gallium vacancies ($\mathrm{V_{Ga}^{3-}}$), making their generation energetically favorable[11,22,40,43,46] and shifting Fermi energy level toward the valence band. Electrostatic attraction between positively charged $\mathrm{Si_{Ga}^{+}}$ donors and negatively charged $\mathrm{V_{Ga}^{3-}}$ acceptors can lead to the formation of electrically active defect $\mathrm{Si_{Ga}V_{Ga}^{2-}}$ complexes. The pairing of these oppositely charged defects reduces the overall Coulombic energy of the system.[2] The interplay between donor incorporation and compensating defect formation leads to pronounced transient maxima of $\mathrm{Si_{Ga}V_{Ga}}$ and $\mathrm{Si_{As}}$ defects at the undoped/doped GaAs interface [Fig. 5(a)]. These defect maxima reflect a temporary imbalance as the material dynamically accommodates new doping conditions. As growth continues deeper into the doped region, the influence of the underlying intrinsic/undoped layer gradually diminishes. With continuous silicon doping, defect populations have more time to redistribute, allowing compensating defects to partially recombine or migrate away. Thus, the number of $\mathrm{Si_{Ga}V_{Ga}}$ and $\mathrm{Si_{As}}$ moves toward lower bulk equilibrium concentration. When doping is abruptly terminated at the second interface, transitioning back to intrinsic conditions, a similar transient adjustment occurs. The sudden drop in donor concentration triggers a defect redistribution. Again, compensating defects, such as $\mathrm{Si_{Ga}V_{Ga}}$ and $\mathrm{Si_{As}}$, briefly peak to accommodate this rapid shift, creating a symmetrical but slightly more pronounced defect profile compared to the first interface. The less pronounced peak in the deeper, buried interface has undergone prolonged thermal annealing during the growth of subsequent layers, which could explain partial relaxation and redistribution of defects, reflecting a state closer to equilibrium conditions. The undoped region lacks the necessary thermodynamic driving force (low electron concentration and higher defect formation energies), effectively preventing diffusion of silicon and its associated defects into the undoped layer. Consequently, sharp defect maxima and an Si redistribution occur only within the doped region. The use of the ULIE-SIMS technique provides a unique capability to quantitatively track individual silicon-based defect species during abrupt doping transitions and thermal treatments in GaAs:Si structures. This approach, offering subnanometer depth resolution, opens new paths for exploring dopant incorporation, compensation mechanisms, and defect diffusion in GaAs systems.

2. Annealing-induced defect transformations

a. Si_p. To the best of our knowledge, the diffusion parameters of the Si pair have been quantitatively extracted from depth-resolved experimental data for the first time. The observation that the profile broadens with temperature while the total dose remains constant supports the hypothesis that Si_p diffuses as an intact complex, rather than through dissociation into individual atoms. Several diffusion models have previously addressed the role of Si–Si pairs in GaAs. In one of the earliest models, Greiner and Gibbons proposed that nearest-neighbor Si pairs act as the dominant diffusing species.[48] While our results demonstrate that this assumption does not hold in the case of GaAs:Si at the doping levels investigated, we nonetheless find agreement with the broader concept that Si pairs can act as mobile species, however, with very limited mobility. On the other hand, the Si–V model proposed by Yu *et al.*[4] assumes that Si pairs are immobile and do not contribute to diffusion. Although our findings clearly indicate some degree of Si_2 mobility, the very low concentration of Si involved in forming pairs (less than 0.5% of total Si in our samples) combined with their low diffusion coefficient suggests that their role in an overall dopant redistribution is indeed minimal. This implies that, for epitaxial structures with moderate doping levels, the neglect of Si pair diffusion in simplified models may still yield accurate macroscopic predictions. More recent work,[5] including DFT-based continuum models, has treated Si pairs as both stable and mobile, with second-nearest-neighbor jumps on the Ga sublattice exhibiting energy barriers around 1.84 eV. This qualitative framework aligns well with our experimental observations, which confirm both the stability and limited mobility of Si_p. Notably, our experimentally determined activation energy (1.63 eV) is not far from the predicted migration barrier. Another recent work[9] investigated the Si behavior at higher doping levels ($2–4 \times 10^{19}$ atoms/cm^3). High angular resolution electron channeling x-ray spectroscopy (HARECXS) and x-ray absorption fine structure (XAFS) studies, supported by DFT calculations, revealed the formation of neutral Si_{Ga}–Si_{As} dumbbell configurations, stabilized through covalent bonding and consistent with our identification of Si–Si pairs. Their results also indicated that the presence of adjacent V_{As} enhances the stability of such complexes.[9] Although our study focuses on a lower doping regime, we observe that even annealing at 1000 °C, which resulted in As-poor conditions, did not cause a significant increase in the Si_p concentration. This suggests that the initial As-rich growth conditions could limit the population of Si pairs. It should be emphasized that the Si_2 depth profile was obtained by directly probing Si–Si bonds, without relying on additional material-based assumptions used for other defect species (Si_{Ga}, $Si_{Ga}V_{Ga}$). This makes their quantification robust against the presence of additional silicon defects, such as $Si_{Ga}V_{As}$, which have been reported in some studies.[23,24] Hence, the applied methodology provides a foundation for future, systematic studies on the formation mechanisms of Si_2 pairs as a function of growth and thermal processing conditions.

b. Si_{As}. Annealing induces a significant increase in the concentration of Si_{As} defects. The Si_{As}/Si_{Ga} ratios in the central region of our samples (0.06–0.076 for 800–950 °C) agree with the average value reported by Ishida *et al.* for MBE-grown epitaxial layers doped at comparable levels and annealed at 580 °C, which yielded a value of 0.077.[18] In that study, ratios approaching 0.2 were observed for n-type GaAs substrates with carrier concentrations above $1.5 \times 10^{18}\ cm^{-3}$; this value is comparable to the interface-adjacent Si_{As}/Si_{Ga} ratios measured in our annealed samples. These results indicate that post-annealing, MOVPE-grown layers can exhibit Si_{As}/Si_{Ga} ratios similar to those in MBE-grown material under comparable doping conditions.

Despite the elevated temperature, the diffusion tails of Si_{As} extending beyond the originally doped region remain similar across all annealing temperatures, suggesting that Si_{As} is considerably less mobile than Si_{Ga}. However, conclusions regarding Si_{As} diffusivity remain limited, as the observed redistribution cannot be fully explained by diffusion. The profile evolution points to the involvement of additional mechanisms, such as site exchange processes or defect-mediated transformations, that can contribute to the changes in the Si_{As} distribution. Moreover, the redistribution observed within the doped layer is consistent with DFT calculations, which predict relatively low energy barriers for Si jumps between Ga and As sublattices.[5]

For the 1000 °C annealed sample, the flattening of the Si_{As} depth profile may be related to changes in defect energetics under As-poor conditions. At this temperature, the substantial As deficiency in the doped layer could increase the availability of As sites throughout much of the layer, providing a driving force for $Si_{Ga} \rightarrow Si_{As}$ site-switching and tending to reduce spatial variations in the Si_{As} distribution.

It should be noted that Si_{As} is detected via the Ga_3Si signal, which reflects silicon atoms bonded to gallium atoms rather than the presence of vacancies themselves. Therefore, even in an As-deficient matrix, ULIE-SIMS likely qualitatively captures the spatial distribution of Si_{As} defects. While it cannot be fully verified whether the proportionality between the Ga_3Si signal and Si_{As} remains unchanged under these extreme conditions, the continued validity of the empirical relationship between As_3Si, Ga_3Si, and carrier concentration at 1000 °C suggests that, even in this regime, the measured signals reflect a quantitative relationship between all charged defects, including Si_{As}. The potential influence of the As-poor environment on the calibration parameter cannot be excluded, and if such effects are confirmed in future studies, the already estimated quantification of Si_{As} at 1000 °C would need to be revisited.

c. Si_{Ga}. While the overall redistribution of Si_{Ga} resembles thermal diffusion, the presence of a local increase in the Si_{Ga} concentration in the center of the profile at intermediate annealing temperatures [Fig. 9(c)] suggests partial local transformation of Si atoms from compensating defect configurations, such as Si_{As} or $Si_{Ga}V_{Ga}$, back into substitutional donor-active Si_{Ga} sites. Considering the observed changes in the Si_{As} concentration and the coupled evolution of Si_{Ga} and Si_{As} during annealing, it is plausible that sublattice exchange reactions play a key role in the redistribution dynamics. DFT calculations predict that the energy barrier for a Si atom to migrate from an As site to a Ga sublattice site is approximately 0.4 eV, while the reverse process requires only ~0.1 eV.[5] Although our calculations neglect the minor, non-Fickian contribution from defect transformations, the experimentally determined activation energy for Si_{Ga} diffusion [$E_a = 0.595 \pm 0.082$ eV; Fig. 8(c)] falls within a comparable range, suggesting that sublattice exchange may be the dominant mechanism in the diffusion behavior of Si_{Ga} in the nominally doped region.

Despite these complex redistribution dynamics, the net effect of annealing is not an increase in dopant activation. On the contrary, the Si_{Ga} concentration generally decreased upon annealing, which suggests that annealing under the studied conditions does not facilitate dopant activation; rather, the role of Si_{Ga} as a donor becomes suppressed compared to the as-grown state. Notably, the As_3Si signal increases upon annealing in the nominally doped region. The contrasting trend between the As_3Si signal intensity [Fig. 2(d)] and the actual Si_{Ga} concentrations [Fig. 9(c)] underscores the need for careful interpretation. Both structurally similar Si_{Ga} and $Si_{Ga}V_{Ga}$ defects contain silicon-arsenic bonds and contribute to the As_3Si signal, precluding a simple proportionality to just one species.

The sharp decrease in the Si_{Ga} concentration observed at 1000 °C [Fig. 8(b)] is attributed to arsenic loss during high-temperature annealing, which alters the defect energetics and promotes the transformation of substitutional Si_{Ga} into other configurations under As-poor conditions. We note, however, that previous studies have reported the formation of electronically relevant concentrations of V_{As}-related defects in As-deficient GaAs, a species not included in our current defect model, leading to a misinterpretation of the Si_{Ga} profile in this extreme case. Further work on systems with a confirmed As-poor defect landscape is needed to clarify how variations in the underlying defect populations influence the measured ULIE-SIMS signals and, in turn, impact the applicability and accuracy of the present quantification framework.

d. $Si_{Ga}V_{Ga}$. The observed redistribution of $Si_{Ga}V_{Ga}$ with temperature indicates a shift in the dominant compensation mechanism across different regions of the sample. Within the nominally doped region, $Si_{Ga}V_{Ga}$ remains the primary compensating species. However, in the adjacent undoped regions, $Si_{Ga}V_{Ga}$ and Si_{As} appear to contribute in a more comparable manner. The spatial correlation between these two defects suggests an interdependence in their redistribution behavior.

Within the framework adopted in this work, the pronounced increase in the calculated $Si_{Ga}V_{Ga}$ concentration at 1000 °C in the central region of the doped layer is interpreted as evidence for enhanced formation of this defect complex under arsenic-deficient conditions, likely occurring at the expense of isolated Si_{Ga} donors. However, if additional defects, such as $Si_{Ga}V_{As}$, were to form in significant concentrations at this temperature, the derived Si_{Ga} and $Si_{Ga}V_{Ga}$ profiles would no longer represent the true defect distribution, and the underlying assumptions regarding total silicon content and the set of defects influencing the carrier concentration would require revision to establish a more suitable framework. Because $Si_{Ga}V_{As}$ shares the same Si-As bonding motif as both Si_{Ga} and $Si_{Ga}V_{Ga}$, its potential contribution to the As_3Si signal cannot be excluded on the basis of the present ULIE-SIMS data. Investigating the possible influence of such defects, therefore, remains an open question for future studies. The observed agreement between ULIE-SIMS-derived and ECV carrier profiles at 1000 °C may, therefore, indicate either that neutral $Si_{Ga}V_{As}$ defects, if present, do not significantly influence the As_3Si signal, leaving assumption from Eq. (2), effectively valid, or that the empirical carrier–signal relationship captures the net charged-defect landscape, including possible contributions from unmodeled defects or defect–vacancy interactions, without explicit identification of all participating species. Distinguishing between these scenarios, and clarifying the possible influence of $Si_{Ga}V_{As}$ or related complexes, remains an open topic for future investigation.

Altogether, these detailed defect-resolved analyses highlight the complex interplay between diffusion and site-specific redistribution processes. The insights gained from our depth-resolved ULIE-SIMS methodology set the stage for a broader understanding of silicon-based defect dynamics and provide a foundation for optimizing doping strategies and defect control in advanced epitaxial semiconductor technologies.

B. Outlook for defect analysis using ULIE-SIMS

While several techniques have contributed significantly to our understanding of dopant behavior and defect formation in GaAs:Si, each comes with inherent limitations that hinder comprehensive defect-specific depth profiling. The approach presented in this study addresses a critical gap between atomic-scale identification and device-scale relevance.

Atomic-resolution methods, such as scanning tunneling microscopy (STM), have proven highly effective in identifying individual point defects in GaAs, including Si_{Ga} and Si_{As}.[2,13,18–20] In certain cases, complementary techniques, such as positron annihilation spectroscopy (PAS), have been used to provide additional insight, particularly for vacancy-related species.[13,22] However, while STM excels in atomic-scale defect identification, it is inherently a surface-sensitive technique and not optimized for quantitative depth profiling. Moreover, obtaining statistically meaningful defect concentrations typically requires a large number of localized measurements across multiple surface regions,[2,18] making comprehensive, device-scale profiling time-consuming and experimentally demanding.

On the other hand, spectroscopic techniques, including infrared absorption and X-ray absorption spectroscopy (XAS), provide element-specific insight into local coordination and chemical bonding environments, typically averaged over relatively large volumes compared to surface-sensitive methods. These methods have been successfully used to study bonding configurations of Si-based complexes in GaAs:Si.[8,49] However, their inherently macroscopic sampling leads to a loss of depth resolution, making it challenging to study nanoscale variations or interfacial effects.

Traditional SIMS combined with ECV has long served as a workaround to infer compensation levels by comparing total dopant concentration with the measured carrier concentration profile.[50] This approach is invaluable for determining device-relevant electrical properties but lacks insight into why compensation occurs. Without knowledge of the specific defect species responsible, optimizing activation strategies becomes a process of trial and error. The feedback loop between material processing and device performance remains incomplete.

In contrast, ULIE-SIMS offers a uniquely integrated solution. It combines the bonding sensitivity of spectroscopy with the depth resolution, enabling subnanometer quantitative profiling of chemically distinct defect species, including Si_{Ga}, Si_{As}, $Si_{Ga}V_{Ga}$, and Si_p. It also provides an alternative route to carrier concentration profiling, particularly when ECV is limited by surface roughness[51] or depth calibration uncertainties. In our implementation, the depth scale is directly tied to the total Si profile, ensuring repeatability. While

ECV remains indispensable for establishing calibration coefficients in systems not yet extensively studied, ULIE-SIMS offers high depth resolution and robustness against surface-quality variations.

Our results demonstrated that thermal annealing, commonly employed to improve dopant activation, did not enhance the concentration of substitutional Si_{Ga} donors. Instead, it facilitated the redistribution of silicon into compensating configurations—including Si_{As} and $Si_{Ga}V_{Ga}$ complexes—ultimately limiting electrical activation. This confirms that while conditions used in this study are insightful for studying fundamental defect behavior, they are not optimal for maximizing activation, underlining the necessity of systematic studies to develop more effective activation protocols, specifically by exploring the defect dynamics within the lower, technologically relevant temperature range. Crucially, the ULIE-SIMS methodology introduced in this work enables such optimization to be guided by defect-specific insights, moving beyond traditional approaches relying solely on free-carrier measurements.

ULIE-SIMS capacity to distinguish specific defect species with depth resolution makes it particularly valuable in systems where conventional electrical techniques fall short. Beyond GaAs-based structures, this approach could be effectively applied to other doped semiconductors, including wide-bandgap materials, such as β-Ga_2O_3, where standard electrochemical methods are often restricted.[29] By enabling direct access to chemically specific depth profiles, this technique could potentially become a platform for advancing defect characterization across diverse material classes.

While this study demonstrates the potential of ULIE-SIMS for defect-resolved profiling, its current quantitative implementation relies on an assumed defect landscape for the material under investigation. This requirement can limit applicability in cases where the dominant defects are not well known or may vary significantly with the growth method, doping regime, or post-growth processing. In this regard, there is strong potential for synergy between ULIE-SIMS and complementary defect-identification methods, such as STM or PAS, which can provide validation of defect species. Broader studies on GaAs:Si with varied defect landscapes in material type, growth, and processing would clarify how defect changes influence ULIE-SIMS signals and the robustness of quantification. In the present work, we analyze epitaxial GaAs:Si structures, but other preparation routes could yield different initial defect configurations that would further test the method's generality. It is also important to note that our quantification framework is not absolute: for example, the calibration parameter β_1 relating the Ga_3Si signal to Si_{As} is estimated internally within the model and would benefit from independent cross-validation in future dedicated studies. Moreover, advancing the predictive capabilities of ULIE-SIMS will require a deeper theoretical and experimental understanding of the complex polyatomic ion formation processes, which at present are treated empirically. Addressing these areas will strengthen both the interpretative power and the general applicability of ULIE-SIMS for defect profiling in semiconductors.

Overall, ULIE-SIMS emerges as a powerful diagnostic tool for refining annealing protocols, optimizing activation strategies, and evaluating defect-driven degradation mechanisms. By providing access to quantitative depth profiles of specific defect species, this method opens new pathways for feedback-driven process optimization and more targeted approaches to doping and defect control in advanced semiconductor structures.

VI. CONCLUSIONS

This study demonstrates a comprehensive methodology for defect-resolved quantitative profiling of silicon-based species in GaAs:Si using ULIE-SIMS. By combining polyatomic signal analysis with a robust calibration framework grounded in electrochemical capacitance–voltage measurements, we establish a route to simultaneously determine the quantitative depth distributions of Si_{Ga}, $Si_{Ga}V_{Ga}$, Si_{As}, and Si_p defects with subnanometer resolution.

We introduce and validate a calibration model in which the ULIE-SIMS signals As_3Si and Ga_3Si serve as weighted indicators of charged-defect species contributing to the free-carrier concentration. The empirical relation derived from this model enables accurate carrier profiling even in samples where a traditional ECV technique is challenged by surface roughness, inhomogeneities, or potentially complex doping architectures.

The developed methodology was applied to a multilayer GaAs/GaAs:Si/GaAs structure subjected to post-growth annealing across a range of temperatures (800–1000 °C). Within the defect framework adopted in this work, results revealed evidence of defect-specific redistribution mechanisms, including the thermally activated diffusion of Si_{Ga} and Si_p species, the sublattice exchange between Si_{Ga} and Si_{As}, and enhanced $Si_{Ga}V_{Ga}$ complex formation under arsenic-deficient conditions. Activation energies and diffusivity coefficients for selected defects were extracted directly from the measured depth profiles, providing new experimental insights for future modeling efforts. Notably, the ability to access both bulk and interface regions enabled a detailed examination of doping transitions, revealing pronounced peaks in compensating defects at the boundaries of the doped region. These findings suggest that local variations in the Fermi level and defect formation energy during epitaxial growth drive transient defect dynamics. While these conclusions are drawn within the specific defect landscape assumed here, we acknowledge that the quantitative framework depends on this assumption, and that further work on systems with systematically varied defect configurations will be important to test the method's generality.

Overall, this work establishes ULIE-SIMS as a powerful tool for spatially resolving electrically active and compensating defects in doped semiconductors, representing significant advancement over conventional profiling methods. By mapping the quantitative distributions of Si-based defects, it lays the groundwork for more detailed investigations into doping behavior and contributes both to the development of experimental strategies aimed at minimizing electrical compensation in device-relevant structures and to the advancement of models describing defect dynamics.

Furthermore, the future prospects outlined in this study highlight the broad potential of this methodology to impact a wider range of semiconductor systems, reinforcing its value as a versatile platform for advancing defect engineering and materials design.

SUPPLEMENTARY MATERIAL

See the supplementary material for details on calibration and validation of ULIE-SIMS for carrier concentration profiling, technical details of ECV measurements, discussion of interpretative limitations and applicability boundaries of ULIE-SIMS carrier concentration analysis, details of the model used for defect diffusion analysis, including discussion of total Si diffusion, and error estimation of calibration parameters. Supplementary material 2 contains ULIE-SIMS signal datasets for C1–C6 calibration samples.

ACKNOWLEDGMENTS

This work was supported by the National Centre for Research and Development, Poland (Project No. LIDER/8/0055/L-12/20/NCBR/2021) and by Research Ireland under Grant Nos. 18/EPSRC–CDT/3585, 12/RC/2276_P2,22/FFP-P/11530, and 22/FFP-A/10930, GOIPD/2024/395.

AUTHOR DECLARATIONS

Conflict of Interest

The authors have no conflicts to disclose.

Author Contributions

Adrianna Rejmer: Conceptualization (equal); Formal analysis (lead); Investigation (lead); Methodology (lead); Validation (lead); Visualization (lead); Writing – original draft (lead); Writing – review & editing (lead). **Ayse Ozcan-Atar:** Investigation (supporting); Writing – review & editing (supporting). **Walery Kołkowski:** Investigation (supporting). **Iwona Pasternak:** Investigation (supporting). **Sylwia Kozdra:** Formal analysis (supporting); Writing – review & editing (supporting). **Andrzej Materna:** Investigation (supporting). **Włodzimierz Strupiński:** Resources (equal); Supervision (supporting). **Emanuele Pelucchi:** Resources (equal); Supervision (supporting). **Paweł Piotr Michałowski:** Conceptualization (equal); Formal analysis (supporting); Investigation (supporting); Methodology (supporting); Resources (equal); Supervision (lead); Validation (supporting); Writing – review & editing (supporting).

DATA AVAILABILITY

The data that support the findings of this study are available from the corresponding author upon reasonable request.

REFERENCES

[1] T. Mano, H. T. Miyazaki, T. Kasaya, T. Noda, and Y. Sakuma, "Double-sided nonalloyed Ohmic contacts to Si-doped GaAs for plasmoelectronic devices," ACS Omega **4**, 7300–7307 (2019).

[2] C. Domke, P. Ebert, M. Heinrich, and K. Urban, "Microscopic identification of the compensation mechanisms in Si-doped GaAs," Phys. Rev. B **54**, 10288–10291 (1996).

[3] M. Greiner and J. Gibbons, "Diffusion and electrical properties of silicon-doped gallium arsenide," J. Appl. Phys. **57**, 5181–5187 (1985).

[4] S. Yu, U. M. Gösele, and T. Y. Tan, "A model of Si diffusion in GaAs based on the effect of the Fermi level," J. Appl. Phys. **66**, 2952–2961 (1989).

[5] M. Reveil and P. Clancy, "Resolving the mystery of the concentration-dependence of amphoteric dopant diffusion in III–V semiconductors," Acta Mater. **186**, 555–563 (2020).

[6] S. Schuppler, D. L. Adler, L. N. Pfeiffer, K. W. West, E. E. Chaban, and P. H. Citrin, "Can electrical deactivation of highly Si-doped GaAs be explained by autocompensation?," Appl. Phys. Lett. **63**, 2357–2359 (1993).

[7] J. Maguire, R. Murray, R. C. Newman, R. B. Beall, and J. J. Harris, "Mechanism of compensation in heavily silicon-doped gallium arsenide grown by molecular beam epitaxy," Appl. Phys. Lett. **50**, 516–518 (1987).

[8] S. Schuppler, D. L. Adler, L. N. Pfeiffer, K. W. West, E. E. Chaban, and P. H. Citrin, "Identifying and quantifying point defects in semiconductors using x-ray-absorption spectroscopy: Si-doped GaAs," Phys. Rev. B **51**, 10527–10538 (1995).

[9] G. Saito, A. Ishizuka, M. Ohtsuka, S. Ito, T. Okajima, and S. Muto, "Dopant site analysis of heavily Si-doped GaAs using a combination of electron microscopy and synchrotron radiation," J. Appl. Phys. **137**, 025703 (2025).

[10] T. Laine, K. Saarinen, J. Mäkinen, P. Hautojärvi, C. Corbel, L. N. Pfeiffer, and P. H. Citrin, "Observation of compensating Ga vacancies in highly Si-doped GaAs," Phys. Rev. B **54**, R11050–R11053 (1996).

[11] J. E. Northrup and S. B. Zhang, "Dopant and defect energetics: Si in GaAs," Phys. Rev. B **47**, 6791–6794 (1993).

[12] M. Holtz, T. Sauncy, T. Dallas, and S. Massie, "Effect of pressure on defect-related emission in heavily silicon-doped GaAs," Phys. Rev. B **50**, 14706–14709 (1994).

[13] J. Gebauer, R. Krause-Rehberg, C. Domke, P. Ebert, and K. Urban, "Identification and quantification of defects in highly Si-doped GaAs by positron annihilation and scanning tunneling microscopy," Phys. Rev. Lett. **78**, 3334–3337 (1997).

[14] M. Uematsu and K. Maezawa, "Compensation mechanism in heavily Si-doped GaAs grown by MBE," Jpn. J. Appl. Phys. **29**, L527 (1990).

[15] Y. G. Chai, R. Chow, and C. E. C. Wood, "The effect of growth conditions on Si incorporation in molecular beam epitaxial GaAs," Appl. Phys. Lett. **39**, 800–803 (1981).

[16] J. H. Neave, P. J. Dobson, J. J. Harris, P. Dawson, and B. A. Joyce, "Silicon doping of MBE-grown GaAs films," Appl. Phys. Solids Surf. **32**, 195–200 (1983).

[17] P. Blood, "Capacitance-voltage profiling and the characterisation of III–V semiconductors using electrolyte barriers," Semicond. Sci. Technol. **1**, 7–27 (1986).

[18] N. Ishida, T. Mano, and T. Noda, "Atomic-scale characterization of highly doped Si impurities in GaAs using scanning tunneling microscopy," Appl. Surf. Sci. **583**, 152373 (2022).

[19] J. F. Zheng, X. Liu, N. Newman, E. R. Weber, D. F. Ogletree, and M. Salmeron, "Scanning tunneling microscopy studies of Si donors (Si Ga) in GaAs," Phys. Rev. Lett. **72**, 1490–1493 (1994).

[20] G. Lengel, R. Wilkins, G. Brown, and M. Weimer, "Tunneling microscopy of point defects on GaAs(110)," J. Vac. Sci. Technol. B **11**, 1472–1476 (1993).

[21] R. T. Chen and W. G. Spitzer, "Si-defect concentrations in heavily Si-DOPED GaAs: Annealing-induced changes-II," J. Electron. Mater. **10**, 1085–1129 (1981).

[22] V. Bondarenko, J. Gebauer, F. Redmann, and R. Krause-Rehberg, "Vacancy formation in GaAs under different equilibrium conditions," Appl. Phys. Lett. **87**, 161906 (2005).

[23] C. Domke, P. Ebert, and K. Urban, "Changes of defect and active-dopant concentrations induced by annealing of highly Si-doped GaAs," Phys. Rev. B **57**, 4482–4485 (1998).

[24] J. Gebauer, R. Krause-Rehberg, C. Domke, P. Ebert, K. Urban, and T. E. M. Staab, "Direct identification of As vacancies in GaAs using positron annihilation calibrated by scanning tunneling microscopy," Phys. Rev. B **63**, 045203 (2001).

[25] P. P. Michałowski, "Probing a chemical state during ultra low impact energy secondary ion mass spectrometry depth profiling," J. Anal. At. Spectrom. **34**, 1954–1956 (2019).

[26] A. Wójcik, W. Kolkowski, I. Pasternak, W. Strupiński, S. Kozdra, and P. P. Michałowski, "Electrically active and hydrogen passivated Zn in GaAs/AlGaAs specifically distinguished during secondary ion mass spectrometry depth profiling," J. Anal. At. Spectrom. **36**, 178–184 (2021).

[27] A. Ozcan-Atar, A. Gocalinska, P. P. Michałowski, M. Johnson, J. O'Hara, B. Corbett, A. Rejmer, F. Peters, D. D. Vvedensky, A. Zangwill, G. Juska, and

E. Pelucchi, "Why 'Zn diffusion' is not always diffusion: Surface physics and a 40-year-old epitaxy problem," Appl. Surf. Sci. **688**, 162360 (2025).

[28] S. Sun, C. Wang, S. Alghamdi, H. Zhou, Y. Hao, and J. Zhang, "Recent advanced ultra-wide bandgap β-Ga_2O_3 material and device technologies," Adv. Electron. Mater. **11**, 2300844 (2025).

[29] K. Sasaki, M. Higashiwaki, A. Kuramata, T. Masui, and S. Yamakoshi, "Si-ion implantation doping in β-Ga_2O_3 and its application to fabrication of low-resistance ohmic contacts," Appl. Phys. Express **6**, 086502 (2013).

[30] V. Dimastrodonato, L. O. Mereni, R. J. Young, and E. Pelucchi, "AlGaAs/GaAs/AlGaAs quantum wells as a sensitive tool for the MOVPE reactor environment," J. Cryst. Growth **312**, 3057–3062 (2010).

[31] P. P. Michałowski, M. Gębski, P. Śpiewak, W. Kołkowski, I. Pasternak, W. Głowadzka, M. Wasiak, T. Czyszanowski, and W. Strupiński, "Artifact-free secondary ion mass spectrometry profiling of a full vertical cavity surface emitting laser structure," Measurement **225**, 114003 (2024).

[32] J. Hunter, "Introductory chapter," in *Secondary Ion Mass Spectrometry: Fundamentals, Advancements and Applications*, edited by P. P. Michałowski (Royal Society of Chemistry, 2025), p. 3.

[33] R. Bock, P. P. Altermatt, and J. Schmidt, "Accurate extraction of doping profiles from electrochemical capacitance voltage measurements," in *Proceedings of the 23rd European Photovoltaic Solar Energy Conference, EU-PVSEC 2008* (WIP-Renewable Energies, Munich, 2008), Vol. 23, pp. 1510–1513.

[34] E. Peiner, A. Schlachetzki, and D. Krüger, "Doping profile analysis in Si by electrochemical capacitance-voltage measurements," J. Electrochem. Soc. **142**, 576–580 (1995).

[35] K. A. Grossklaus and J. M. Millunchick, "Mechanisms of nanodot formation under focused ion beam irradiation in compound semiconductors," J. Appl. Phys. **109**, 014319 (2011).

[36] L. Bischoff, R. Böttger, K.-H. Heinig, S. Facsko, and W. Pilz, "Surface patterning of GaAs under irradiation with very heavy polyatomic Au ions," Appl. Surf. Sci. **310**, 154–157 (2014).

[37] T. E. Haynes, W. K. Chu, T. L. Aselage, and S. T. Picraux, "Initial evaporation rates from GaAs during rapid thermal processing," J. Appl. Phys. **63**, 1168–1176 (1988).

[38] H. Sakaguchi, R. Suzuki, and T. Meguro, "Systematic study on Si and Se doping of MOVPE GaAs," J. Cryst. Growth **93**, 602–606 (1988).

[39] Y. Komatsu, D. Harata, E. W. Schuring, A. H. G. Vlooswijk, S. Katori, S. Fujita, P. R. Venema, and I. Cesar, "Calibration of electrochemical capacitance-voltage method on pyramid texture surface using scanning electron microscopy," Energy Proc. **38**, 94–100 (2013).

[40] G. A. Baraff and M. Schlüter, "Electronic structure, total energies, and abundances of the elementary point defects in GaAs," Phys. Rev. Lett. **55**, 1327–1330 (1985).

[41] A. Chroneos, H. A. Tahini, U. Schwingenschlögl, and R. W. Grimes, "Antisites in III–V semiconductors: Density functional theory calculations," J. Appl. Phys. **116**, 023505 (2014).

[42] K. Wada, "Defects and material processing in compound semiconductors," Appl. Surf. Sci. **85**, 246–252 (1995).

[43] P. A. Schultz and O. A. Von Lilienfeld, "Simple intrinsic defects in gallium arsenide," Model. Simul. Mater. Sci. Eng. **17**, 084007 (2009).

[44] S. Zhang and J. Northrup, "Chemical potential dependence of defect formation energies in GaAs: Application to Ga self-diffusion," Phys. Rev. Lett. **67**, 2339–2342 (1991).

[45] J. K. Kung and W. G. Spitzer, "Si-defect concentrations in heavily Si-doped GaAs: Changes induced by annealing," J. Appl. Phys. **45**, 4477–4486 (1974).

[46] T. Y. Tan, H.-M. You, and U. M. Gösele, "Thermal equilibrium concentrations and effects of negatively charged Ga vacancies in n-type GaAs," Appl. Phys. Solids Surf. **56**, 249–258 (1993).

[47] W. Walukiewicz, "Mechanism of Fermi-level stabilization in semiconductors," Phys. Rev. B **37**, 4760–4763 (1988).

[48] M. E. Greiner and J. F. Gibbons, "Diffusion of silicon in gallium arsenide using rapid thermal processing: Experiment and model," Appl. Phys. Lett. **44**, 750–752 (1984).

[49] W. G. Spitzer and W. Allred, "Local-mode absorption and defects in compensated silicon-doped gallium arsenide," J. Appl. Phys. **39**, 4999–5009 (1968).

[50] T. Suzuki, H. Goto, N. Sawaki, H. Ito, and K. Hara, "Autocompensation in Si planar doped GaAs," Appl. Surf. Sci. **82–83**, 103–108 (1994).

[51] M. Heinrich, H. Hidayat, Z. Hameiri, B. Hoex, and A. G. Aberle, "Dopant profiles of laser-doped multicrystalline silicon wafers from electrochemical capacitance-voltage measurements," in *Proceedings of the 27th European Photovoltaic Solar Energy Conference, EU-PVSEC* (WIP-Renewable Energies, Munich, 2012), Vol. 27, pp. 1285–1288.